

## Prestack simultaneous inversion to predict lithology and pore fluid in the Realgrunnen Subgroup of the Goliat Field, southwestern Barents Sea

Honore Dzekamelive Yenwongfai<sup>1</sup>, Nazmul Haque Mondol<sup>2</sup>, Jan Inge Faleide<sup>3</sup>, and Isabelle Lecomte<sup>4</sup>

### Abstract

**1** An integrated multidisciplinary workflow has been implemented for quantitative lithology and fluid predictions from prestack angle gathers and well-log data within the Realgrunnen Subgroup in the Goliat Field, southwestern Barents Sea. We have first performed a qualitative amplitude-variation-with-angle (AVA) attribute analysis to assess the spatial distribution of lithology and fluid anomalies from the seismic data. A simultaneous prestack elastic inversion was then carried out for quantitative estimates of the P-impedance and  $V_P/V_S$  ratio. Probability distribution functions, a priori lithology, and fluid class proportions extracted from well-log training data are further applied to the inverted P-impedance and  $V_P/V_S$  seismic volumes. The AVA qualitative analysis indicates a class IV response for the top of the reservoir, whereas anomalies from the AVA attribute maps agree largely with the clean sand probabilities predicted from the Bayesian facies classification. The largest misclassification in the lithology classification occurs between shaly sands and shales. A mixed lithology and fluid classification indicates a smaller degree of overlap and allows for the discrimination of hydrocarbon sands. Integration of a qualitative AVA analysis and a quantitative Bayesian probability approach helps in constraining the depositional facies variability within the Realgrunnen Subgroup. Finally, a possible influence of tectonic activity during the deposition of the Realgrunnen reservoir is inferred based on the facies distribution maps.

### Introduction

The profit margins for oil and gas companies are narrowing down as exploitation costs increase and oil and gas prices decrease. As a result, it is even more important to use quantitative seismic characterization schemes to reduce financial and operational risks. Lithology and fluid prediction from all available data is the ultimate goal for subsurface hydrocarbon exploration. Reservoir drainage in field development is also dependent on this information. The increase in computing power coupled with major advances in seismic acquisition and processing routines make quantitative interpretations from seismic data even more reliable. Subtle stratigraphic features contained in the seismic data may be completely overlooked if quantitative methods are not incorporated in seismic reservoir characterization workflows.

Seismic reflection data result from contrasts in elastic properties at layer interfaces in the subsurface. Over the past few decades, seismic inversion and amplitude-variation-with-offset (AVO) or amplitude-variation-with-angle

(AVA) analysis have become more routine tasks in seismic reservoir characterization workflows. The AVA phenomenon has long been identified (Zoeppritz, 1919). However, it became routinely applicable after the mathematical basis for the variation of reflection amplitude with angle was simplified over the years (e.g., Aki and Richards, 1980; Shuey, 1985; Smith and Gidlow, 1987; Fatti et al., 1994; Verm and Hiltermann, 1995; Goodway et al., 1997). The Aki-Richards equation describes a linearized AVA intercept, gradient, and curvature approximation to the Zoeppritz equation. The curvature term is more important for very far offsets. Shuey's (1985) approximation is valid for small incident angles up to 30° and provides a way of estimating the change in Poisson's ratio across an interface based on an estimate of the AVA intercept and gradient. Smith and Gidlow (1987) approximation provides an alternate two-parameter AVO that is valid for larger incident angles than Shuey's (1985) approximation. Smith and Gidlow (1987) also introduce the fluid factor that was then implemented in the detection of gas sands using the Geostack technique (Fatti

Part of this paper has been presented during the 78th EAGE Conference and Exhibition in Vienna, June 2016 (DOI: 10.3997/2214-4609.201600964).

<sup>1</sup>Statoil ASA, Stavanger, Norway and University of Oslo, Oslo, Norway. E-mail: h.d.yenwongfai@geo.uio.no.

<sup>2</sup>University of Oslo, Oslo, Norway and Norwegian Geotechnical Institute (NGI), Oslo, Norway. E-mail: m.n.h.mondol@geo.uio.no.

<sup>3</sup>University of Oslo, Oslo, Norway. E-mail: j.i.faleide@geo.uio.no.

<sup>4</sup>University of Oslo, Oslo, Norway and University of Bergen, Bergenhus, Bergen, Norway. E-mail: isabelle.lecomte@uib.no.

Manuscript received by the Editor 1 July 2016; revised manuscript received 20 November 2016. This paper appears in *Interpretation*, Vol. 5, No. 2 (May 2017); p. 1–22, 19 FIGS., 1 TABLE.

<http://dx.doi.org/10.1190/INT-2016-0109.1>. © 2017 Society of Exploration Geophysicists and American Association of Petroleum Geologists. All rights reserved.

et al., 1994). An intercept-gradient crossplot analysis (Castagna and Swan, 1997) is an important tool used to classify gas sands. This classification is an extension of the earlier classification of gas sands proposed by Ruth-erford and Williams (1989). Verm and Hilterman (1995) first demonstrate the power of AVA crossplot rotation to improve lithology and fluid discrimination. This is done by coordinate rotation of a crossplot of normal incidence and Poisson's ratio reflectivity. Through this method, AVA data can be rotated such that subtle class II reservoirs can be imaged as class III reservoirs after a 45° coordinate rotation.

AI in seismic interpretation is strictly valid only for a zero-offset section. For nonnormal incident angles, mode conversion occurs at layer interfaces, and a nonzero offset elastic impedance (EI) can be computed (Connolly, 1999). Some limitations in the EI method are later addressed by Whitcombe et al. (2002), and the concept is applied to extended EI (EEI). EEI is a scaled version of the EI attribute, and its computation requires a theoretical rotation angle ( $\chi$ ) in the intercept-gradient crossplot space. The rotation angle can have values ranging from  $-90^\circ$  to  $+90^\circ$ . The interpretation advantage of EEI attributes comes from the fact that specific rotation angles correspond to elastic parameters, such as lambda-nu-rho (LMR) (Goodway et al., 1997) and the compressional-to-shear velocity ( $V_P/V_S$ ) ratio. The LMR parameters are known to be good lithology and fluid discriminators.

Seismic inversion is not a new technique. It uses an estimated interface property (reflectivity) between successive layer boundaries to derive effective elastic properties to the layers. Several types of seismic inversion algorithms exist, e.g., relative impedance inversion (Lancaster and Whitcombe, 2000), simultaneous AVO inversion (Hampson et al., 2005), and joint facies-based impedance inversion (Kemper and Gunning, 2014). The inversion could either be poststack or prestack, deterministic or stochastic, based on the type of input seismic data and whether or not a background low-frequency model is needed. Rock-physics models can then be used to relate the elastic properties derived from the inversion to actual rock properties. The theory behind the use of rock-physics templates (RPTs) is initially proposed by Dvorkin and Nur (1996) and Ødegaard and Avseth (2004).

Previous studies in the same study area by Dario et al. (2013) combine the Bayesian linearized inversion by Buland and Omre (2003) with statistical rock-physics modeling to infer petrophysical properties (such as porosity) from the seismic. Unlike a pure deterministic simultaneous inversion that provides one set of elastic parameters from the seismic, a Bayesian linearized approach provides a probability estimate of the elastic properties. This is an added advantage of the Bayesian linearized inversion methods compared with a purely deterministic model-based simultaneous inversion approach.

In our workflow, we first qualitatively assess spatial AVA anomalies in the target zone subsequent to applying

a Bayesian lithology and fluid classification (based on simple petrophysical cutoffs) to the deterministic elastic inversion results. In general, simultaneous inversion schemes try to preserve the background relationship among AI, SI, and density  $\rho$  during the inversion process as opposed to independently inverting for these parameters.

The studied Goliat Field is located in blocks 7122/7 and 7122/8 in the Norwegian sector of the Barents Sea (Figure 1). The field is located approximately 85 km southeast of the Snøhvit gas field and 85 km northwest of Hammerfest, mainland Norway. The discovery well (7122/7-1) was drilled in 2000. The field has been developed using a floating production, storage, and offloading vessel connected to several subsea templates. The water depths in this part of the Barents Shelf range between 360 and 420 m. The Goliat Field is among the few oil finds compared with the more dominant gas-prone discoveries within the Barents Sea area. This is the first oil field to come on stream (March 2016) on the Norwegian Barents Sea despite an exploration history spanning over three decades.

The Realgrunnen Subgroup and the Kobbe Formation (within the Sassendalen Group) represent the two main reservoir units targeted in this field, and they are located at depths of approximately 1100 and 1800 m below sea level, respectively. These Triassic-Early Jurassic reservoir units are strongly compartmentalized. Minor gas caps have been observed at different stratigraphic levels. Other reservoir units present are the Snadd and Klappmyss Formations (within the Kapp Toscana Group and Sassendalen Group, respectively). As a result of low reservoir pressures, produced water and gas are reinjected into the reservoir to provide pressure support and optimize recovery over time. The expected lifetime of the field is more than 15 years.

The primary objective of this study is to quantitatively map the distribution of sands within the Realgrunnen Subgroup using prestack simultaneous inversion and petrophysical well data from seven (six exploration and one appraisal) wells as the main input. The secondary objective is to use AVA attribute analysis to qualitatively highlight the hydrocarbon and lithology anomalies. Quantitative fluid prediction in areas with over-consolidated rocks, such as the uplifted Barents Shelf area, is challenging. This is due to a reduced fluid sensitivity in seismic, as a result of a stiffened rock framework.

## Geologic setting

Two major continental collisions and their resultant orogenies characterize the early history of the Barents Shelf: (1) the older Caledonian orogeny and (2) the younger Uralian orogeny, which represents one of the last major collision elements in Permian-Triassic times leading to the creation of Pangea. These major orogenies dominate the basement substructure in the basin, and it probably influenced its later structural evolution (Glørstad-Clark et al., 2010). After the orogenic phases, periods of extension then ensued in the Barents Sea

area, leading to a collapse of the previously formed orogenic belts and progressive breakup of Pangea during Late Paleozoic and Mesozoic times. The result of the extension is a complex mosaic of structural highs, rift basins, and platforms across the Barents Shelf (Johansen et al., 1993).

The major structural elements within the Western Barents Shelf have been documented by several authors (Gabrielsen et al., 1990; Gudlaugsson et al., 1998; Faleide et al., 2008). Three main geologic provinces have been identified in the Western Barents Shelf (Faleide et al., 2008), each of which is separated by major fault zones (Figure 2). One of these fault zones is the Troms-Finnmark Fault Complex (TFFC). The Goliat Field is structurally located in a restraining bend in the TFFC and forms a prominent roll-over anticline. The TFFC is an old zone of weakness with listric normal faults (Faleide et al., 1984; Dore, 1995).

The Late Palaeozoic on the Barents Shelf is dominated by carbonates and evaporites in the Devonian, Carboniferous, and Permian (Figure 3). However, the Triassic and younger sediments are represented by a dominant clastic sediment succession. These two distinct sets of lithology at different periods in the stratigraphic evolution of the Barents Shelf point to a tectonic and a climatic influence (Worsely et al., 1986). The Triassic in the Western Barents Sea was a relatively tectonically quiet period (Riis et al., 2008). Thick Triassic clastic units are observed throughout the Barents Shelf (Mørk et al., 1989). According to palaeogeographic reconstructions of the Triassic in the Western Barents Sea (Glørstad-Clark et al., 2010), multiple sediment sources exist. However, the dominant sediment input came from northwest-prograding clastic wedges sourced from the Uralian orogenic belt to the east and southeast.

The Realgrunnen Subgroup (it lithostratigraphically belongs to the Kapp Toscana Group) was deposited during Norian to Bajocian times and comprises the Fruholmen, Tubåen, Nordmela, and Stø Formations (Figure 3). The shallower Nordmela and Stø Formations are eroded and are not observed in any of the exploration and appraisal wells in the Goliat Field area. The studied area has been subjected to Cenozoic uplift like most of the Barents Sea. The amount of uplift could be up to 1500 m, based on vitrinite reflectance data from a suite of wells around the study area (Ohm and Karlsen, 2008). This makes the reservoir

overconsolidated for any given depth observed today and has a negative impact on seismic fluid sensitivity.

Thickness variations within the Realgrunnen Subgroup range from approximately 65 to 120 m, based on the exploration and appraisal wells. There is a general coarsening upward sequence in the wells. The base of this reservoir (base of the Fruholmen Formation) has a thick shale unit, which can be correlated across the wells in the area. The top of the reservoir usually has the best sands with porosities up to 35%.

## Database and methods

A multidisciplinary approach is required to quantitatively map the distribution of reservoir sands within a heterogeneous, uplifted, and segmented reservoir zone such as the Realgrunnen Subgroup. Information from

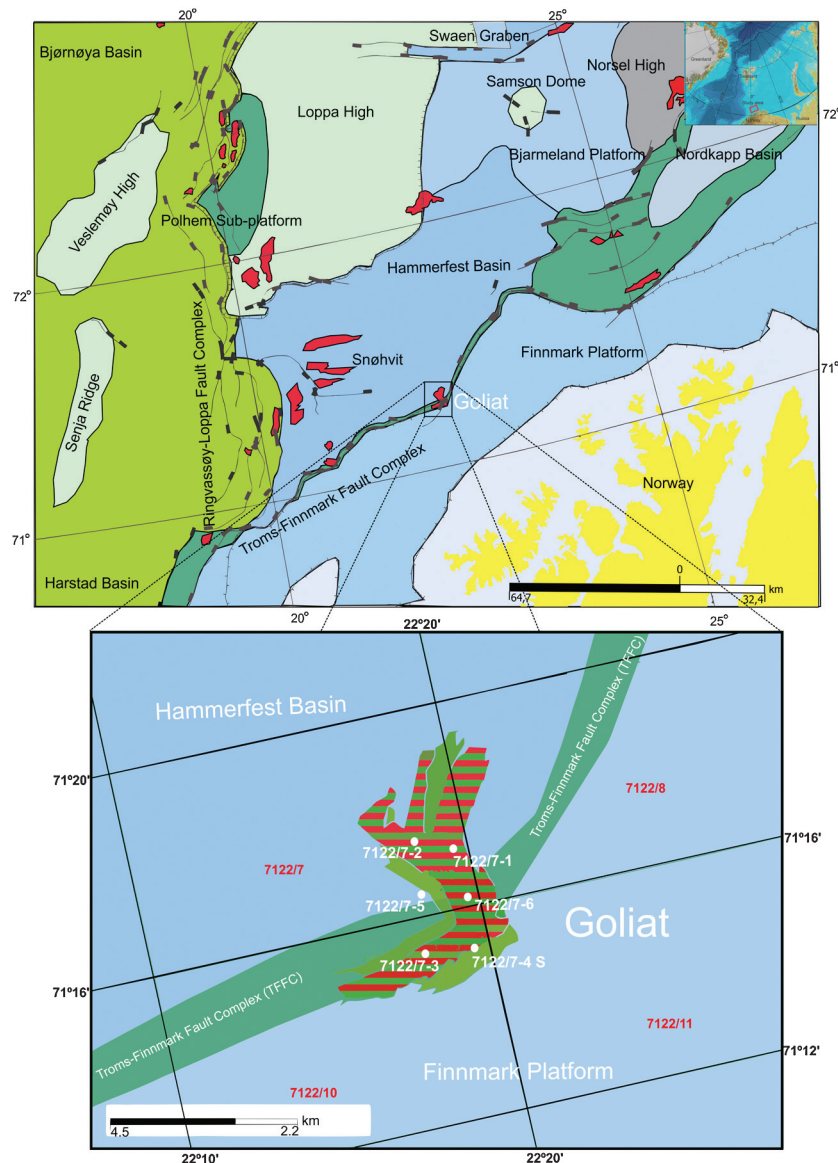


**Figure 1.** Location map for the Goliat Field (adapted from NPD factMaps) in the Norwegian sector of the Barents Sea. The field is cut by the Troms-Finnmark Fault Complex within blocks 7122/7 and 7122/8.



geology, petrophysics, rock physics, and geophysics at different scales are all integrated. Wireline logs, multi-azimuth (MAZ) 3D seismic data, prestack depth-migrated (PSDM) velocities, and horizon interpretations necessary for this study were provided by the PL229 license.

The input long-offset MAZ 3D seismic data were acquired in 2009 using ten 4000 m long streamers. Each of the three acquisition azimuths (127°, 67°, and 7° N), covered a full-fold area of approximately 209,000 m<sup>2</sup>. The bin size for the data is 25 × 6.25 m<sup>2</sup>. The MAZ seismic data were then rotated to a common azimuth (127° N), i.e., the same as the older surveys. The stacked MAZ 3D seismic data have a 160 nominal fold compared with 48 in the older standard 3D surveys in the same study area. This implies a superior and improved stacking process with better signal-to-noise ratios. The input seismic data were processed using AVO-compliant workflows (Buia et al., 2010), making quantitative amplitude interpretations more reliable. The MAZ 3D data also provide a much better illumination of the complex compartmentalized target reservoirs. Details about MAZ seismic data acquisition, processing, weighting of the partial stacks, and data improvements are provided in Buia et al. (2010). Three weighted angle stacks (Figure 4) were used as inputs to the simultaneous prestack elastic inversion. The seismic has been processed with a reversed polarity such that a drop in impedance is represented as a peak on the seismic data. This can be seen in the P-impedance (AI) log on the near-angle stack section. The

superimposed synthetic trace in the mid-angle stack illustrates the quality of the well-to-seismic tie over the target zone. The sand flag is plotted in yellow in the far-angle stack.

There is a clear decrease in the seismic amplitudes from the near-angle stack to the far-angle stack and a corresponding decrease in the frequency bandwidth. This decrease in bandwidth with the increasing offset can easily be seen from the angle-dependent statistical wavelet response (Figure 5). The near-angle (10°–25°), mid-angle (25°–39°), and far-angle (39°–59°) partial stacks were of good quality and corresponded to mid-angles of 17°, 32°, and 45°, respectively. Prestack angle gathers were subsequently generated using the mid-angles from the partial stacks.

As mentioned earlier, the well database consists of seven wells. Two of these wells are water wet within the Realgrunnen Subgroup, whereas oil and minor gas accumulations are observed in the other wells. Several development wells have already been drilled, but they are not available for this study. The key logs (Figure 5) used as input for the inversion were the compressional velocity  $V_P$ , S-wave velocity  $V_S$ , and bulk density  $\rho_b$ . Two of the wells have measured  $V_S$  logs. A suite of other depth-corrected formation evaluation logs (e.g., gamma ray, shale volume  $V_{sh}$ , porosity [PHIE], and resistivity) has been used for lithology discrimination. Minor edits were performed to the sonic logs to ensure reliable estimates of AI logs in the time domain. Figure 6 illustrates the multidisciplinary workflow presented in this paper (Yenwongfai et al., 2016). This workflow can be subdivided into three major steps: (1) qualitative AVO attribute analysis, (2) petrofacies characterization and rock-physics diagnostics, and (3) simultaneous prestack amplitude inversion.

### Qualitative AVO attribute analysis

The qualitative AVO attribute analysis was done by comparing AVA synthetic models from the reference well (7122/7-3) with the actual AVA model obtained from the angle gathers. AVA synthetic traces from 1D reflectivity models were generated using the Zoeppritz algorithm (Zoeppritz, 1919). The amplitudes from the top and base reservoir sands interface were then extracted and curve fitted to a linearized three-term Aki and Richards (1980) approximation on an amplitude-angle crossplot. The intercept and gradient for the selected interface can then be graphically estimated.

The AVA intercept and gradient attributes are rarely used independently. A crossplot and rotation angle projections of these attributes provide indeed more information than either alone. A three-term AVO attribute analysis was

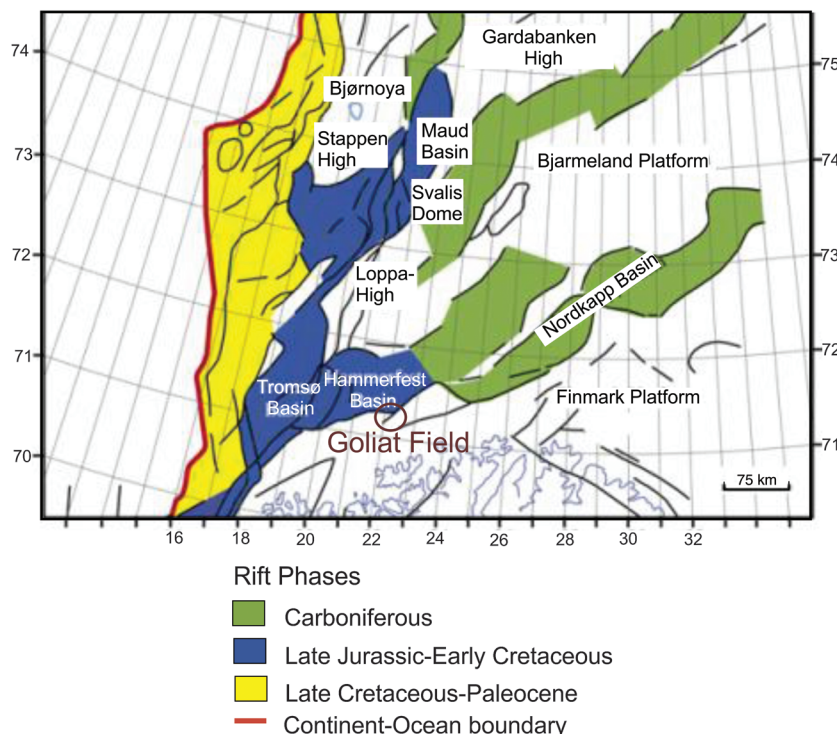


**Figure 2.** Main structural elements in the Western Barents Sea. The focus of tectonic activity through time is indicated by the different colors (modified after Faleide et al., 2008).



subsequently performed due to the good-quality large-offset coverage of the MAZ data, with the far angles exceeding 30°. However, only combinations of the extracted AVO intercept and gradient terms have been used in the subsequent analysis to qualitatively assess the lithology and fluid anomalies in the data.

Crossplots of the AVO intercept and gradient horizon attribute slices are then combined using a weighted

coordinate rotation to produce new seismic attributes that are tuned to specific elastic and petrophysical parameters of interest (Whitcombe et al., 2002). The optimum data rotation angle is obtained by getting the maximum correlation (Figure 7) of the target well-log curve to the EEI curve and then fine tuning the angle on the AVO intercept and gradient crossplot attribute data slice. The optimum rotation angles derived from the

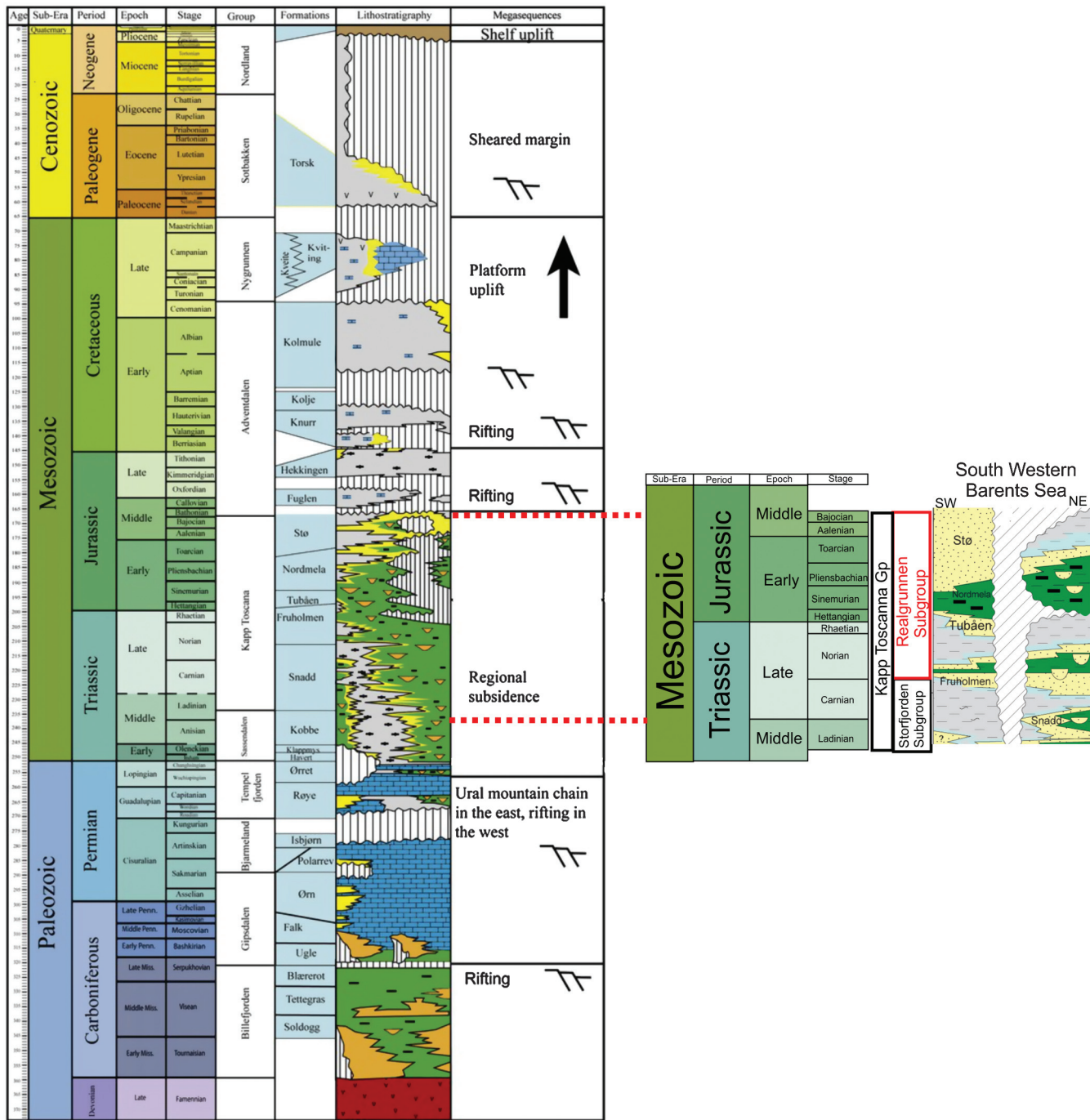


**Figure 3.** Chronostratigraphy of the Norwegian Barents Sea (Glørstad-Clark et al., 2010; Gradstein et al., 2012). The Realgrunnen Subgroup is subdivided into the Stø, Nordmela, Tubåen, and Fruholmen Formations. These formations were deposited during the Late Triassic to Middle Jurassic Epoch. The shallower Nordmela and Stø Formations are absent in the Goliat Field. Other hydrocarbon-bearing intervals, such as the Snadd, Kobbe, and Klappmys Formations, were also deposited during the Triassic period.

wells in many cases will not match the exact seismic optimum projection angle. One reason for this could be a difference in the prestack data scaling compared with the well-derived correlations. However, this served as a good starting point to screen the data.

### Petrofacies characterization and rock physics

The second major step involves establishing a robust lithology classification using well-log data. The lithology and fluid classification has been done in two main steps: (1) Apply a rule-based lithology petrophysical cutoff using reservoir geologic parameters to assess the reservoir quality distribution and (2) combine a second alternate ternary classification with a calibrated rock-physics template to constrain the lithology and fluid classes. The rule-based lithology cutoff uses  $V_{sh}$  and PHIE (corrected for clay volume) to define three

lithology classes, i.e., clean sand, shaly sand, and shale. The second alternate classification uses  $V_{sh}$  and water saturation  $S_w$  to define three lithology and fluid classes, i.e., hydrocarbon sand, brine sand, and background shales. The resulting petrofacies classes shown in Table 1 do not provide any direct information on the depositional facies.

What we actually want from the seismic data are geologic parameters, such as  $V_{sh}$ , PHIE, and  $S_w$ . However, the seismic data respond directly to changes in the effective elastic properties of the layers and indirectly to the geologic variables of interest. RPTs are important tools to help the interpreter relate observations in elastic properties derived from the inversion to rock properties in the wells (Ødegaard and Avseth, 2004). The defined petrofacies are subsequently plotted in terms of different well-derived elastic parameters, such as

AI and the  $V_P/V_S$  ratio. This is a quick feasibility test to assess if the defined lithology and fluid classes show clusters or trends that can potentially be distinguished on the inverted seismic data. A stiff sand model constructed using the Hashin-Shtrikman upper bound also helped in validating the separation of the brine and hydrocarbon sands.

Finally, probability density functions (PDFs) are extracted from all the defined petrofacies classes in the AI and  $V_P/V_S$  crossplot domain. The PDFs are constructed by the smoothing of data points in the crossplot space using an operator (kernel function). The length of the operator determines the amount of smoothing. A large operator length has been used to account for differences in the vertical resolution between the

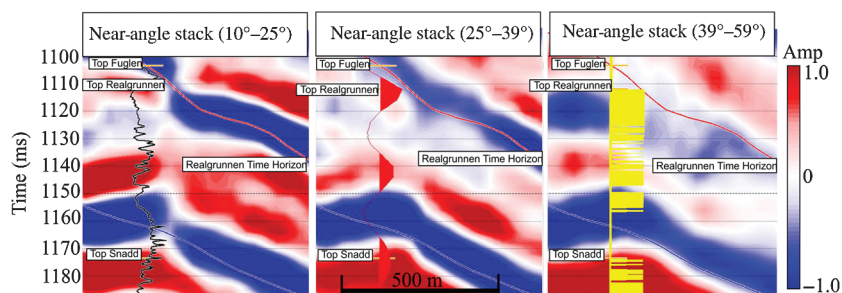


**Figure 4.** Inline section along the 7122/7-3 well, showing the partial angle stacks used in the simultaneous inversion. The top of the reservoir (Top Realgrunnen) is best seen in the near-angle stack section. The top of the reservoir is shown by a drop in P-impedance in the well log (the black curve in the near-angle stack section) from the base of the Fuglen Formation into the Realgrunnen Subgroup. Notice that the seismic is displayed in a reverse-polarity convention (positive amplitudes represent a drop in P-impedance). The synthetic seismic overlay in the mid-angle stack shows the quality of the well tie, whereas the yellow curve in the far-angle stack represents the sand flag.

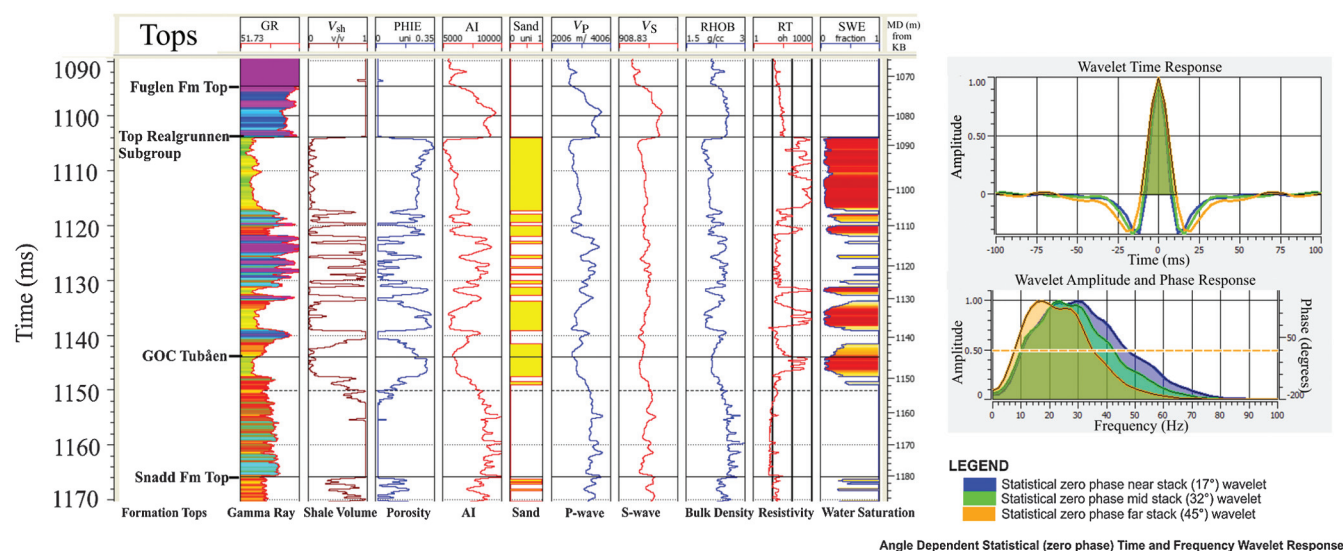


**Figure 5.** Target reservoir interval (7122/7-3 well) and statistical angle-dependent wavelets used in the inversion. The reservoir generally has clean sands at the top, an interbedded sand and shale sequences in the middle, and a dominantly shaly base.

seismic and well data. However, the trade-off associated with increasing the operator length is a corresponding increase in the misclassification of our data set. The optimum operator length is chosen based on cross-validation results. This is a nonparametric statistical classification based on Bayes' theorem. The a priori facies proportions are obtained by analyzing the lithology and fluid classes in the wells. This reduces the nonuniqueness problem of seismic interpretation by making some models more likely than others. The discriminating power of the different elastic parameter combinations are assessed based on confusion matrices and the percentage of misclassified samples.

### Simultaneous prestack amplitude inversion

The third major step in the workflow involves simultaneous prestack inversion (Hampson et al., 2005). The seismic data are band limited. This can clearly be seen in the amplitude spectrum of the statistical wavelet extracted along the inline of the reference well shown in Figure 5. A low-frequency background trend is impor-

tant for two main reasons: (1) to invert for absolute rock properties and (2) to capture the trends in the data set. Without a background model, the inverted result will be relative impedance. The quality of the inversion output is sensitive to the quality of the input gathers, the wavelet processing, the seismic well tie, and the forward modeling of the low-frequency background model. Checkshot-corrected velocity logs and a full-offset seismic vintage have been used as inputs to the well tie.

A good well tie is crucial prior to running the inversion. An angle-dependent statistical wavelet (Figure 5) was extracted from a 1 s time window covering the target interval and used in the well tie. Synthetic seismic was then computed by convolving the statistically extracted wavelet, with a time-reflectivity series derived from impedance variations at the well location. Minor time shifts are then assigned to the checkshot-corrected logs based on the correlation coefficient between the synthetic seismic and the seismic data along the well path.

Once satisfactory well ties are obtained, seismic forward modeling is then performed to create the low-

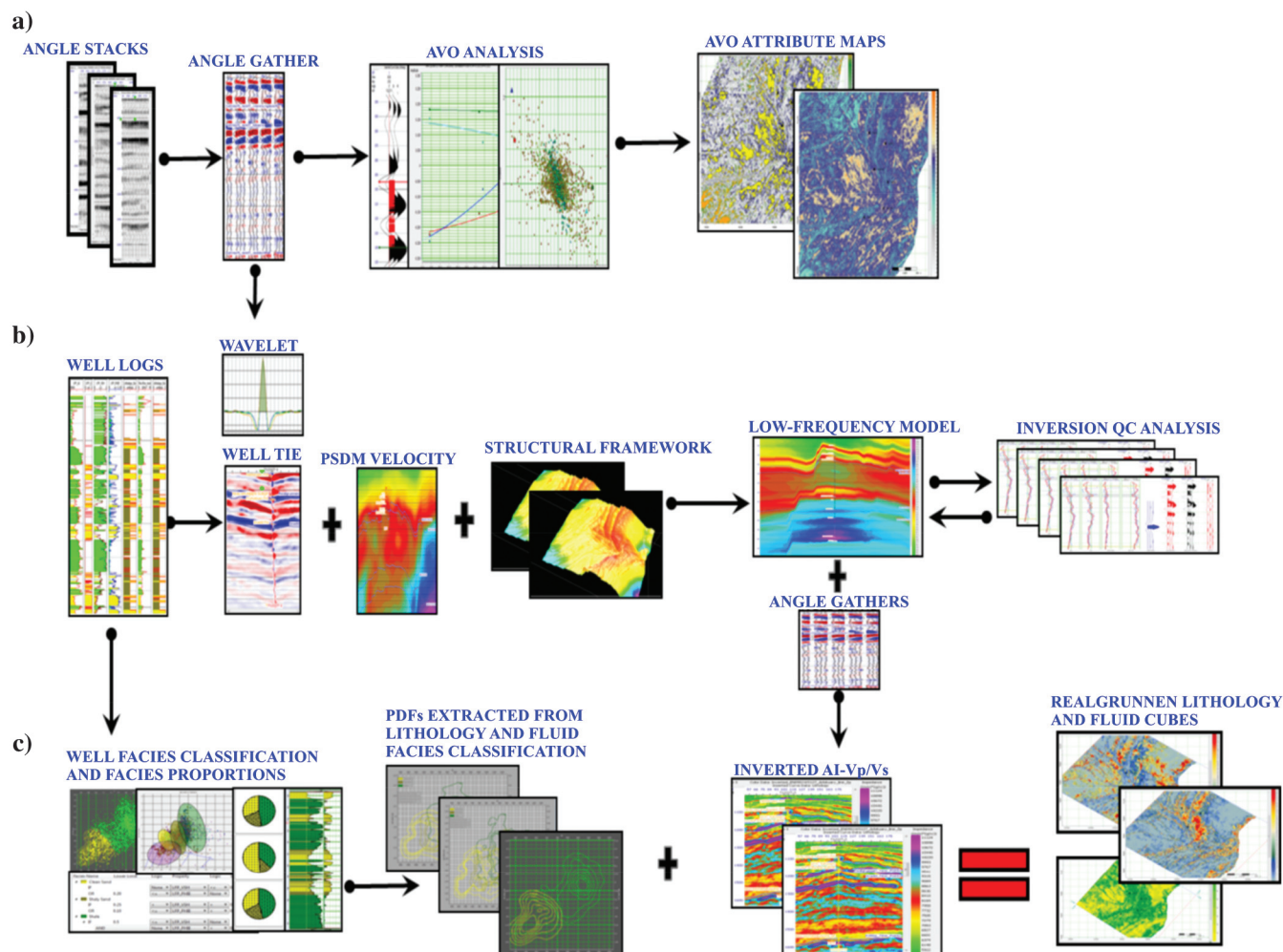


**Figure 6.** Lithology and fluid prediction workflow. The subprocesses in the workflow include: (a) Qualitative AVO-attribute analysis, (b) simultaneous prestack amplitude inversion (Hampson et al., 2005), and (c) petrofacies characterization and rock-physics analysis.



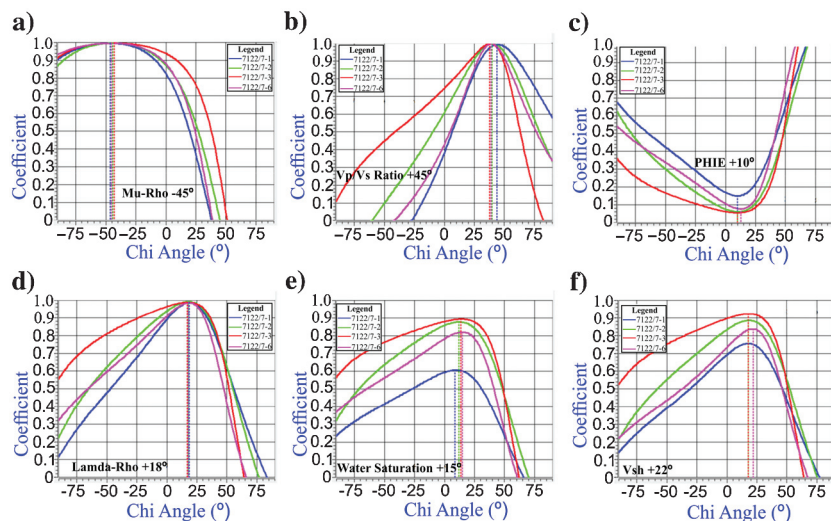


**Figure 7.** EEI correlations to different elastic and petrophysical parameters. (a, b, and d) The elastic parameters show a stronger correlation compared with (c, e, and f) the petrophysical parameters. Also notice the strong negative correlation for (c) PHIE and the weaker correlation for (e) water saturation.

**Table 1. Petrofacies rule-based cut-offs applied to well-log data for facies discrimination. The cut-off between brine and hydrocarbon sands is based on the computed water saturation.**

Petrofacies	Lithology cut-off
Shale	$V_{sh} \geq 0.5$ and $PHIE < 0.10$
Shaly sand	$0.25 < V_{sh} < 0.5$ or $0.10 \leq PHIE < 0.20$
Clean sand	$V_{sh} \leq 0.25$ or $PHIE \geq 0.20$
Petrofacies	Lithology and fluid cut-off
Background (shale)	$V_{sh} \geq 0.5$
Brine sand	$V_{sh} < 0.5$ and $S_w > 0.3$
Hydrocarbon sand	$V_{sh} < 0.5$ and $S_w < 0.3$

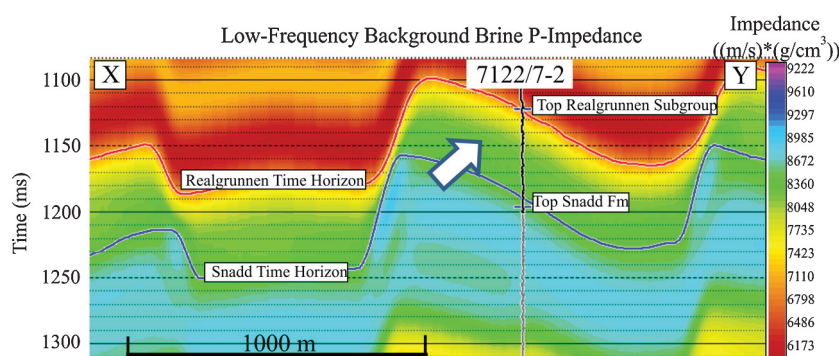


**Figure 8.** Low-frequency background brine P-impedance model inline section. The well and seismic PSDM velocities have been cokriged to achieve this interpolation. The target zone is indicated with the white arrow.

frequency background model. Fluid-replacement modeling (Gassmann, 1951) was performed prior to forward modeling to simulate brine-filled reservoir conditions in all input wells. The brine-substituted logs from the wells are then spatially cokriged with the PSDM velocities to obtain a smooth  $V_P$  interpolation. The interpolation is guided by stratigraphic time surfaces. Low-frequency  $V_S$  and  $\rho$  models are then computed using Castagna et al.'s. (1998) equation (linear relationship between  $V_S$  and  $V_P$ ) and Gardner et al.'s. (1974) equation (relating density to  $V_P$ ). Both equations are valid for brine-filled reservoirs. This forms the basis for introducing linear relationships in building the background low-frequency model. The background linear regression lines are obtained by cross-plotting the corresponding petrophysical well logs and are generally representative of the major trend. The final modeled output traces after lateral interpolation were then passed through a 15 Hz high-cut frequency filter. An inline section of the low-frequency AI model used is shown in Figure 8. Fluid-replacement modeling and frequency filtering are necessary to ensure that anomalies observed in the inverted output come directly from the seismic and not the modeled trend from the well logs.

The inversion algorithm implemented here is fully based on earlier work by Hampson et al. (2005), which builds on previous studies by Simmons and Backus (1996), and Buland and Omre (2003). Both of these prior studies are based on the Aki-Richards equation and invert for reflectivity and impedance, respectively. Fatti et al. (1994) reformulate the Aki-Richards three-term equation and express the P-P reflectivity  $R_{pp}$  at an interface to be related to the sum of the linearized P-wave reflectivity  $P_r$ , S-wave reflectivity  $S_r$ , and density reflectivity  $D_r$  terms as

$$R_{pp}(\theta) = aP_r + bS_r + cD_r, \quad (1)$$

where  $\theta$  is the incident angle;  $a = 1 + \tan^2 \theta$ ,  $b = -8(V_S/V_P)^2 \tan^2 \theta$ , and  $c = -0.5 \tan^2 \theta + 2(V_S/V_P)^2 \tan^2 \theta$ . Each of the reflectivity terms has angle-dependent coefficients. A classic non-simultaneous inversion scheme would then independently poststack invert the  $P_r$ ,  $S_r$ , and  $D_r$  seismic sections from the AVA analysis, provided that there are good-quality far-angle traces up to at least approximately  $40^\circ$ . The poststack inversion output will then be P-impedance, S-impedance, and density. However, doing it this way will ignore the relationship between the output terms.

Introducing a link will reduce the possible number of geologic subsurface models that will give the same elastic response. For example, although there are many geologic model combinations that can have the same P-impedance, there will be much fewer geologic models having the same set of P-impedance, S-impedance, and density. Recognizing this, [Hampson et al. \(2005\)](#) then introduce linear relationships between AI to SI and  $\rho$  to constrain the inversion solution.

[Hampson et al. \(2005\)](#) then modify the [Fatti et al. \(1994\)](#) equation using the small reflectivity approximation for  $P_r$  and the linear background trends to come up with equation 2:

$$T(\theta) = a^1 W(\theta) D \ln(Zp) + b^1 W(\theta) D \Delta(Zs) + c^1 W(\theta) D \Delta \ln(\rho), \quad (2)$$

where  $T(\theta)$  represents a seismic trace at a given incident angle ( $\theta$ );  $W$  and  $D$  represent the angle-dependent wavelet and the derivative matrix, respectively. The terms  $\Delta(\text{SI})$  and  $\Delta \ln(\rho)$  represent deviations from the background linear trends. The original  $a$ ,  $b$ , and  $c$  terms in equation 1 are modified to  $a^1$ ,  $b^1$ , and  $c^1$  with regression coefficients from the background linear trend. The low-frequency information missing in equation 2 comes from the low-frequency model. The final inversion solution is obtained by iteratively updating the initial low-frequency background model. For more details on the mathematical derivations and basis for the simultaneous inversion, we refer the reader to [Hampson et al. \(2005\)](#).

One key advantage of simultaneously inverting for AI, SI, and  $\rho$  is that the relationship between these parameters is captured. This is done by crossplotting their natural logs ( $\ln$ ) (Figure 9) and assuming a linear relationship between AI and the other two parameters (SI and  $\rho$ ).

The inverted AI, SI, and  $\rho$  can be quality checked in two ways. First, we visually examine the correlation between actual AI, SI, and  $\rho$  logs in the wells with the corresponding inverted logs. Second, we check the correlation coefficient and the associated error between the synthetics derived from the inverted logs and the actual seismic at the well location. Finally, we compare the correlation between the synthetic seismic at a blind well (a well not used to constrain the inversion) to the actual seismic extracted from the well location. After several quality control iterations at the well locations, the inversion is applied to the entire 3D conditioned angle gathers to obtain  $V_p$ ,  $V_s$ , and  $\rho_b$  cubes. The PDFs and the a priori facies class proportions from the best well training data are subsequently applied to the inverted seismic volume. The result is thus a sand probability distribution cube for the Realgrunnen Subgroup. The degree of confidence in the facies probability output is dependent on a good inversion in the previous step.

## Results and discussion

In Figure 10, the sand flag (red) is plotted on the synthetic traces from the well. The top reservoir is picked as a trough, and the base reservoir sand corresponds to the black peak in the wiggle display. The actual seismic is plotted adjacent to the synthetic data with a colored display. Positive amplitudes are shown in red, whereas negative amplitudes are shown in blue.

A comparison between the top and base reservoir from the synthetic and actual seismic data indicates the same trends (Figure 10). The top reservoir shows a negative zero-offset reflection (negative AVA intercept) and less negative amplitudes with increasing angle (positive AVA gradient). The synthetic response (curve 1) for the top reservoir in the amplitude-angle crossplot has only negative amplitudes even for the very far offsets. Meanwhile, the actual seismic response for the top reservoir on the same plot (curve 3) shows a change in polarity for angles greater than  $37^\circ$ . The top reservoir response is a typical class IV AVA response (low-impedance reservoir with a positive AVA gradient) plotting in the II quadrant and circled in red (Figure 10). According to [Castagna et al. \(1998\)](#), the key parameter controlling the AVO gradient with increasing offset is the change in  $V_s$ .

The cap rock (Fuglen Formation) is quite stiff, resulting in a drop in the measured  $V_s$  across the cap rock-reservoir interface. This drop implies a negative change in  $V_s$  causing the class IV AVA response. The reservoir sand in contact with the cap rock in the reference well has an average porosity of 25% (coarsening upward sand). A stronger effect of the pore fluid on the elastic properties is expected for a shallow hydrocarbon reservoir with good porosities. However, this is not case as the target reservoir is overconsolidated (stiffer grain framework) at present-day depths because of uplift subsequent to a deep burial. As a result, the pore fluid sensitivity of the seismic wave propagating through the reservoir is decreased.

The base reservoir AVA response is almost a mirror projection, opposite to that of the top reservoir in the amplitude-angle plane. However, there is no polarity change for the base reservoir in the far offsets in the synthetic and actual seismic data at the well position. The polarity change might be due to residual time shifts for the very far offsets even after a trim static correction. This polarity change will be difficult to observe on a full-offset stack because it only occurred in the far angles with very low amplitudes eliminated by stacking. Nevertheless, the overall good correlation between the synthetic and actual seismic in the reference well highlights the quality of the MAZ angle stacks used for simultaneous inversion.

Multiple AVA attributes have been used to qualitatively highlight potential lithology and hydrocarbon anomalies. The scaled Poisson's ratio (sum of the AVA intercept and AVA gradient) for the observed class-IV reservoir is negative for the top reservoir and positive for the base reservoir. The strong amplitudes (green

anomalies) represent strong increases in the Poisson's ratio upon entering the reservoir. The high Poisson's ratio anomalies provide a strong indication for shale in this horizon slice in Figure 11. The scaled Poisson's ratio and the  $V_P/V_S$  ratio show similar sand and shale trends as expected. Shales generally show high  $V_P/V_S$  ratios due to a microstructure that offers less resistance to shearing (lower  $V_S$ ) than sandstones. The  $V_P/V_S$  ratio is even much smaller in hydrocarbon-filled sands compared with brine-filled sands due to a decrease in the incompressibility resulting to a decrease in  $V_P$ . Therefore, an anomalously low  $V_P/V_S$  ratio in the reservoir would result in large changes in the scaled Poisson's ratio attribute across the top reservoir. However, this attribute does not provide a clear distribution for the reservoir sands because it is not possible to say

from this attribute how clean the sands are due to the contributing fluid effects.

Unlike the scaled Poisson's ratio attribute, the scaled S-wave reflectivity attribute is more sensitive to lithology effects and less sensitive to fluid effects in the seismic data. This attribute provides a better resolution for the major depositional trends because the lithology anomalies are more continuous. The reservoir sands are highlighted with stronger positive amplitudes in the S-wave reflectivity. This is expected because sand generally shows a greater resistance to shearing than shale. However, this attribute does not give any quantitative uncertainty information about the probability of sand occurrence. This is the case as well for the attributes derived from angle projections of the AVA intercept and gradient.

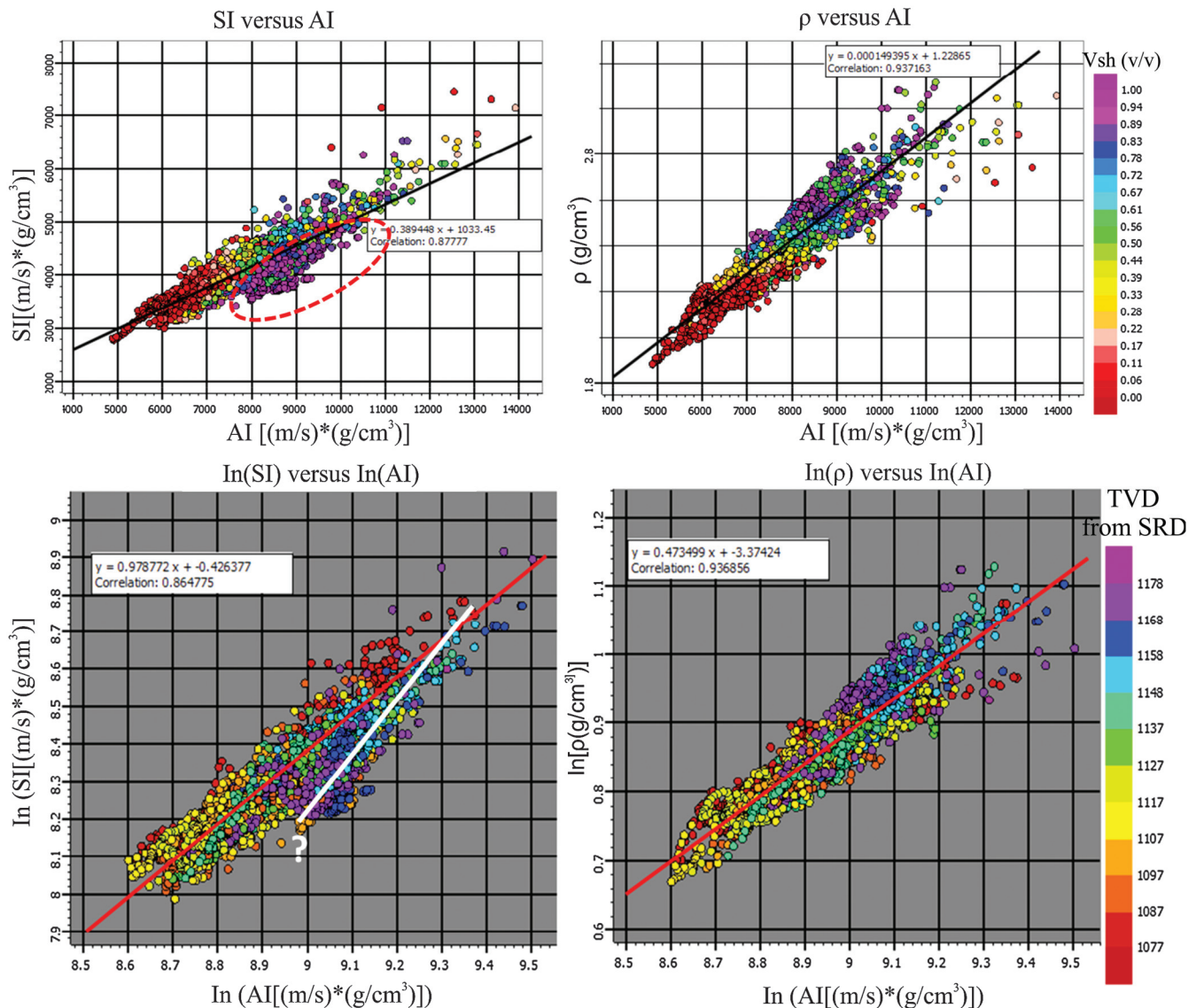


**Figure 9.** Crossplots between AI, SI, and  $\rho$  color coded with shale volume and depth. There is a linear trend in a linear and natural logarithmic (In) scale. The linear regression coefficients between In (AI) to In (SI) and In ( $\rho$ ) are used in the simultaneous inversion to stabilize the background model. A potential subordinate shale trend (white line) can be observed as well from data points within the dotted red oval.



All the chi angle EEI projections in Figure 7 show a positive correlation coefficient except for porosity. This implies that strong positive amplitudes on the porosity reflectivity map (Figure 12) correspond to areas with low effective porosities, and vice versa. For all the other attributes, strong positive amplitudes correspond to high relative values for the target property. However, many of the geologic parameters are correlated and would therefore highlight the same features. The repeatability achieved using different parameters improves the confidence of the qualitative interpretation.

Water saturation (Figure 7) shows a lower correlation and a wider spread in the well-derived correlation coefficients. The lower correlation is possibly indicative of a slightly lower fluid sensitivity for these overconsolidated reservoir sands. The fan area (Figure 12) shows a low MuRho reflectivity pointing toward sandy to silty facies, but with no indication of the degree of uncertainty. The  $V_P/V_S$  reflectivity map in Figure 12 shows a sharper image with negative anomalies indicative of potential sandy-silty facies. The  $V_{sh}$  and PHIE reflectivity maps reveal that the fan system is quite muddy (high  $V_{sh}$ ) and with a low porosity. The same area has strong positive amplitudes for lambda-rho. Lambda-rho is more sensitive to fluids, and the high amplitudes indicate a brine-dominated area. This is supported by the water saturation reflectivity map with the positive bright amplitudes correlating well with high  $S_w$ . A dry well (7122/7-5) has been drilled in to this anomaly in the fan area and validates a brine-filled response for the Realgrunnen.

By integrating information from all the attribute maps in Figure 12, three regions of interest can be distinguished based on their seismic geomorphological character, which point to different depositional styles: (1) a mud-rich fan area (black circle) building out from a southeast-northwest direction bounded by two main faults (purple lines), (2) a braided alluvial plain (white oval) building out to the southwest, and (3) a mud-filled channelized feature (red circle). The mid fan area close to the relay ramp is more sand rich, whereas the distal parts are more shaly. The northeast parts of the attribute slice show a brine-filled and clay-rich channelized feature.

A pitfall of interpreting lithology directly from the AVA attribute maps shown in Figure 12 is potential tuning effects in the data, which can cause thickness changes to be interpreted as changes in reservoir heterogeneity. In addition, potential overburden effects, such as anisotropy and residual gas have not been taken into account. Gas leakage from the reservoir to the overburden is the probable cause of the dimmed seismic amplitudes observed over spe-

cific areas in the Goliat Field. This leads to a dimming of the reservoir amplitudes below these areas.

Figure 13 shows different well-derived P-impedance and  $V_P/V_S$  ratio crossplots color coded with shale volume, water saturation, rule-based facies, and their corresponding PDFs. There is a clear increase in  $V_{sh}$  trend with increasing P-impedance and  $V_P/V_S$  ratio (Figure 13a). The discrimination of the hydrocarbon-bearing sands using the Hashin-Shtrikman upper bound (blue curve) is shown in Figure 13b. Data points plotting above the blue curve are representative of brine-filled sands and background shale. A critical porosity of 35% has been used. Figure 13c and 13e is color coded with lithology and fluid facies classes, whereas Figure 13d and 13f is the corresponding extracted PDFs.

Overall, the pure lithology classification shows a bigger overlap between the classes (Figure 13c) compared with mixed lithology and fluid classification (Figure 13e). Considering just the pure lithology classification, there is a significant degree of misclassification for the shaly sands. The shaly sands show a larger scatter and overlap over a wider area with the clean sands and shales. This can also be observed from the extracted PDFs for the shaly sand class (Figure 13d).

The degree of error in the overlapping PDFs can be described quantitatively using a confusion (error) matrix (Figures 14b and Figure 15b). The diagonal percentages indicate the degree of success of the classification at the wells. For example, in the lithology confusion matrix (Figure 14b), when the classified log predicts

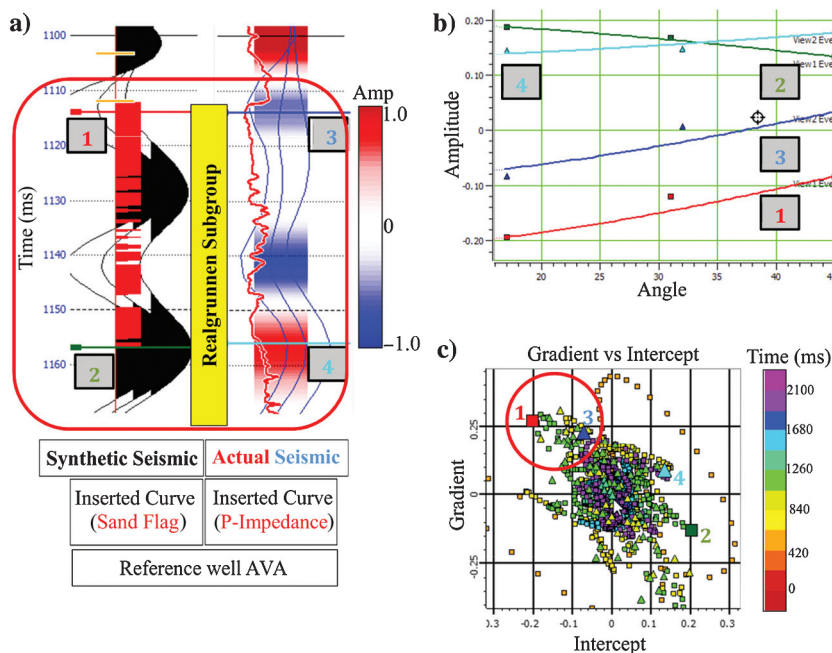


**Figure 10.** Comparison between AVO synthetic gathers and seismic angle gathers along the reference well (7122/7-3). A 180° phase rotation has been applied to the actual seismic in panel (a) to ease visual correlation to the synthetic trace. The top of the reservoir is shown here as a trough and has a positive AVO gradient (curves 1 and 2) in panel (b) typical of a class IV AVA response in the red circle in panel (c).

clean sand, it is correct approximately 78% of the time based on the actual litho-log. The off-diagonal percentages show the degree of confusion in the classified log. The highest confusion occurs when the actual litho-log is shaly sand. In this case, the classified log wrongly predicts this as shale approximately 36% of the time and approximately 43% of the shaly sand data points are misclassified. This implies that a much higher uncertainty is associated with shaly-sand probability maps derived from such a classification.

Based on the facies proportions, the 7122/7-3 and 7122/7-6 wells have the highest proportions of good quality clean sands. This may be indicative of a separate geologic facies, such as distinct coarse braided bars. The pie chart for facies proportions using all the wells (Figure 14b) represents the a priori facies proportion needed for the Bayesian classification. The clean-sand facies make up approximately 32%, whereas the shaly sand and shale facies make up approximately 20% and 48%, respectively.

The mixed lithology and fluid classification confusion matrix shows a better clustering of the defined

classes (Figure 15b). Hydrocarbon sands are correctly classified approximately 81% of the time and misclassified as brine sands approximately 17% of the time. Based on the mixed lithology and fluid confusion matrix, less than 20% of the hydrocarbon sample data points are misclassified. The modeled facies probability at the wells is shown in Figure 15c. There is a positive correlation between the clean-sand class and the hydrocarbon-sand class. The hydrocarbon sands within the Realgrunnen Subgroup appear to be restricted to the clean-sand facies. This is as expected because clean sands generally have lower capillary pressures compared with shaly sands, and they would therefore offer the least resistance for migration and saturation with hydrocarbon fluids.

To quantitatively assess the spatial distribution of different rule-based facies, seismic inverted absolute P-impedance and  $V_P/V_S$  ratios need to be combined with PDFs extracted from the well training data set. The quality of the facies probability maps is dependent on the quality of the inverted traces.

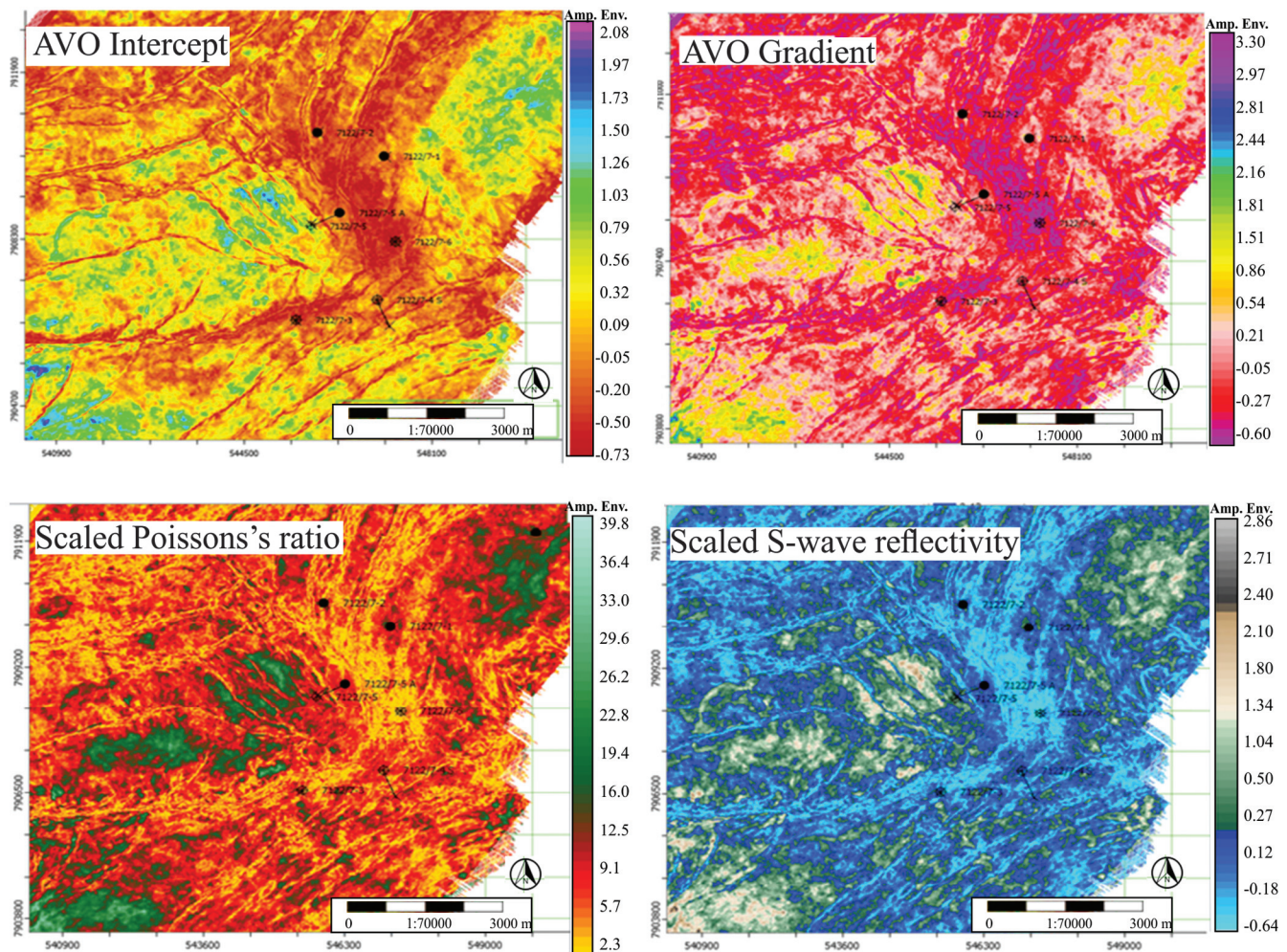


**Figure 11.** Realgrunnen AVA horizon attribute slices of a 10 ms window from the top of the reservoir. High amplitudes in the scaled Poisson's ratio highlight shale dominated parts of the reservoir. The scaled S-wave reflectivity is more sensitive to changes in lithology and less sensitive to fluid effects compared with the scaled Poisson's ratio attribute.



The 7122/7-2 well (Figure 16a) has the largest inversion error (44%), whereas the least error (19%) was observed in the 7122/7-5 well. The inversion error here refers to the difference between the inverted seismic trace at the well location to the actual recorded trace. The correlation window covers the entire Realgrunnen Subgroup, including the Knur Formation (overburden)

and upper parts of the Snadd Formation (underburden) across the wells. Figure 16b shows a comparison between the inverted log (red) and the actual log (blue). The background low-frequency model is also plotted (black) in both tracks. An error of 30% is observed within the target zone (purple rectangle). The good correlation between synthetic traces derived from the in-

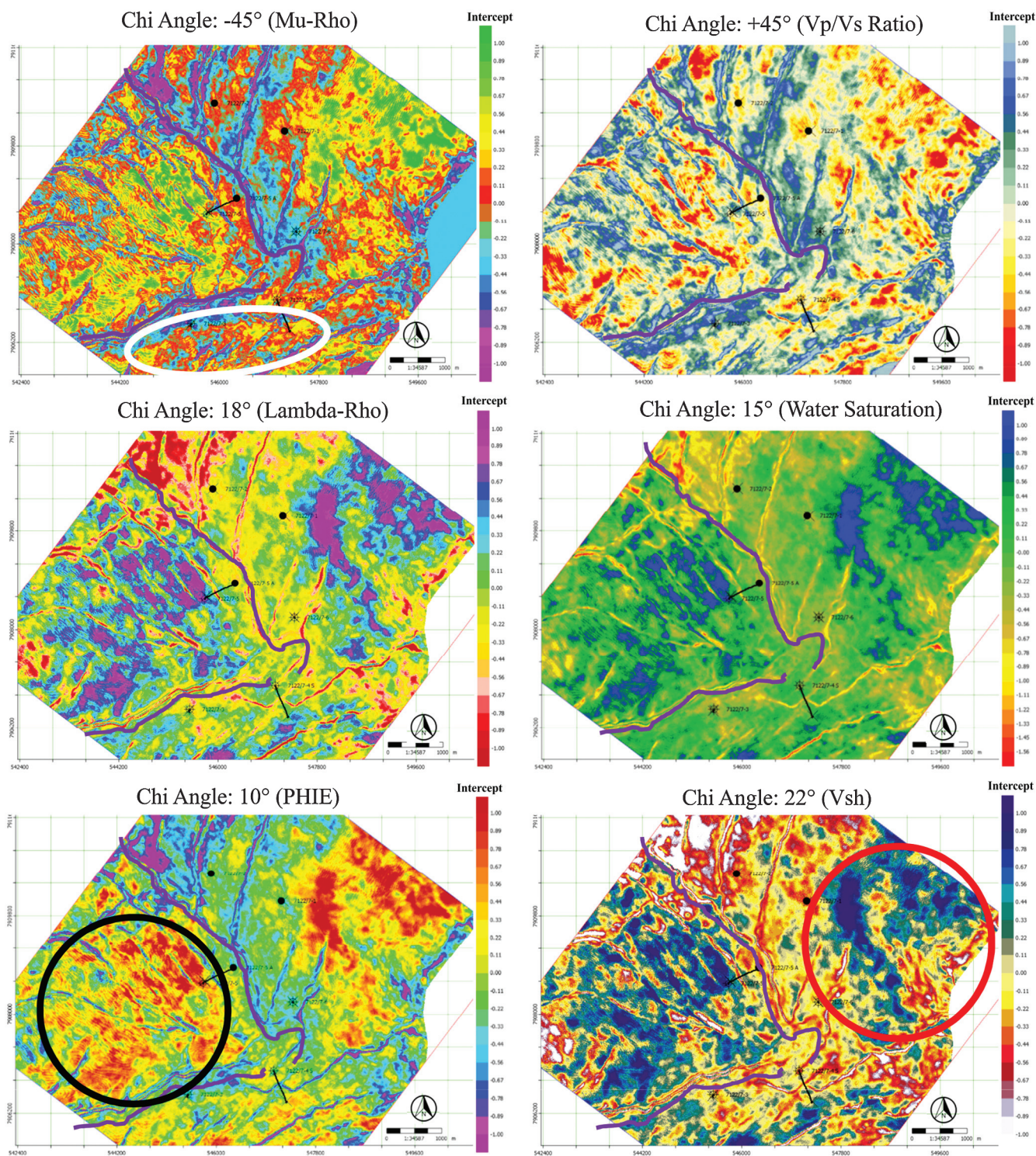


**Figure 12.** The EEL projections of AVA intercept and gradient at different chi angles (see Figure 7 for more information). The maps show similar patterns because these parameters are correlated. A relay ramp fault has been highlighted in purple.



verted results with the actual seismic at the well locations indicates a proper inversion at the well location. However, for the model to be useful, it should be able to

minimize the inversion error at other locations without wells. Figure 16a includes a blind test specified with just inline and crossline coordinates (corresponding to the

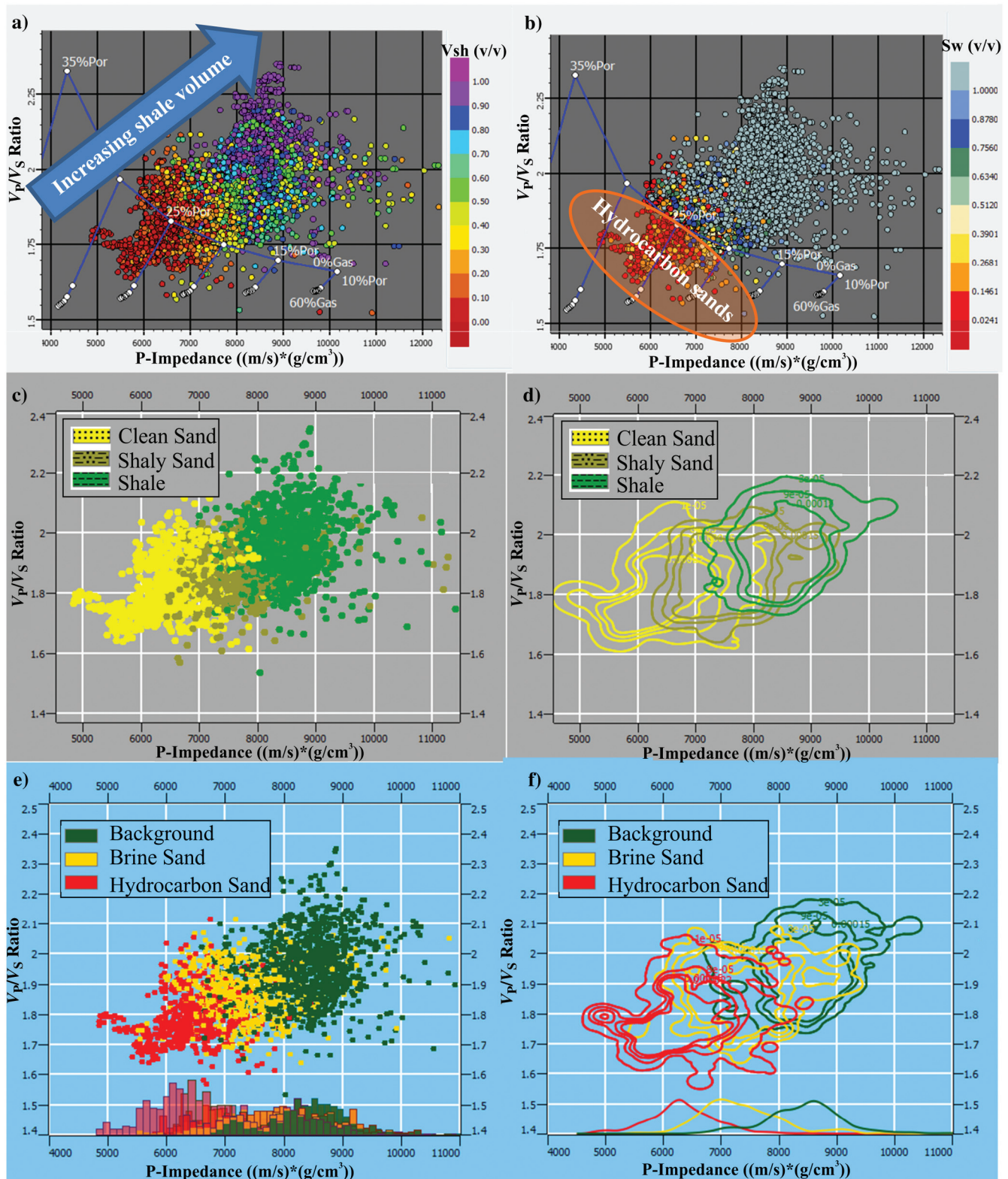


**Figure 13.** Lithology and fluid facies rock-physics P-impedance and  $V_p/V_s$  crossplots. A general trend of increasing shaliness is observed in panel (a). (b) Hydrocarbon sands plot below the calibrated rock-physics template (blue). (d and e) The PDFs extracted from each classification are also displayed alongside (c and e).

7122/7-5A well not used in the inversion), with an inversion error of 26%. A crossplot between the inverted and actual P-impedances color coded with  $V_{sh}$  (Figure 16c) shows a correlation of approximately 0.7. The inversion result was considered good enough for further quantitative interpretation.

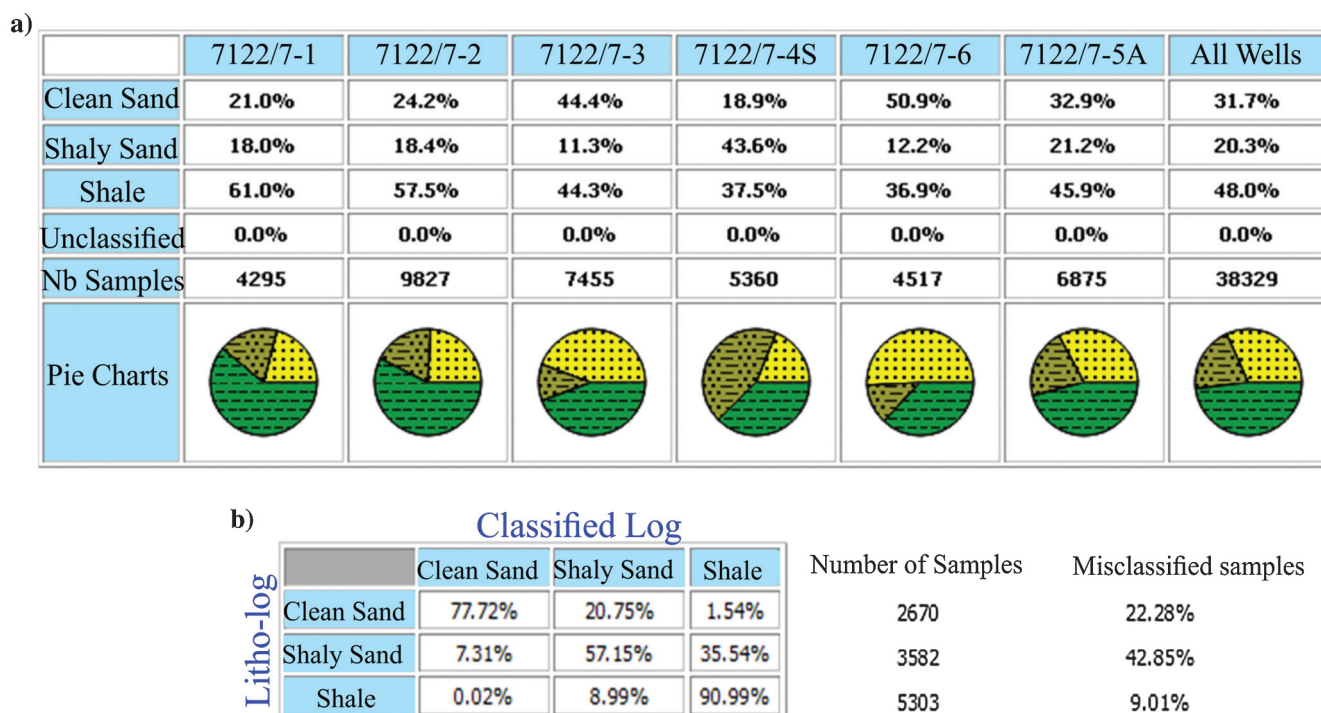
The inverted result along the 7122/7-2 well with the largest inversion error is shown in Figure 17. From these sections, the oil-filled reservoir sands show low AI, Rho, SI, MR (Mu-Rho), and LR (lambda-rho), but so does the source rock (Hekkingen Formation) above the reservoir. This ambiguity is removed by including the  $V_P/V_S$  ratio and LR, which show opposite trends to the reservoir sands. This implies that using AI alone from a poststack inversion would not be adequate enough to separate reservoir sands from the source rock intervals. This is important because multiple source rock intervals exist in the older Triassic units below the Realgrunnen Subgroup. Fortunately, the background shaly units within the target reservoir (Figure 15) do not show this ambiguity. The sand flag (dark yellow curve in Figure 17) is also plotted for visual quality control.

Figure 18 shows the sand probability horizon slice taken 10 ms below the top reservoir and covering a 10 ms window. A braided alluvial plain and fan-complex depositional style can be interpreted from that horizon slice. The sands tend to show a higher probability, in which an accommodation space is created in the half-grabens near the faults. The Goliat South fault segments (around the 7122/7-3 well) are relatively narrower com-

pared with the fault segments in the north and northwest (around the 7122/7-1 and 7122/7-2 wells).

The channels (high sand-probability areas) tend to be closer to faults, and the sands would expect to aggrade vertically. This will result to more ribbon geometries, with poor lateral communication except along the axis of such channels. This could potentially explain the distinct thick sand unit observed at the top reservoir in the 7122/7-3 well. As the half-grabens widen toward the north, braided channels would have fewer lateral structural constraints, and they will therefore migrate more horizontally. This may explain the observed thinner units. The sands in the wider grabens will mostly form braided plain sheet geometries with good lateral communication.

Between the northern and southern segments, there is a significant relay-ramp fault structure. This relay ramp is rerouting the sands to a fan area. The upper V-shape (apex) opening of the fan area shows a greater probability of sand, as expected. The velocity of the alluvial system would be higher at the mouth of the fan where the flow is focused. This would likely result to deposition of sand and coarser sediments first at the apex of the fan. As the flow widens and its velocity drops, finer sediments would then be deposited. Surficial channels can be seen extending from the fan. These channels are also influenced by the structural relief and are most likely responsible for carrying some reservoir sands further out. The areas in between these channels are dominated by shales and some shaly sands. These



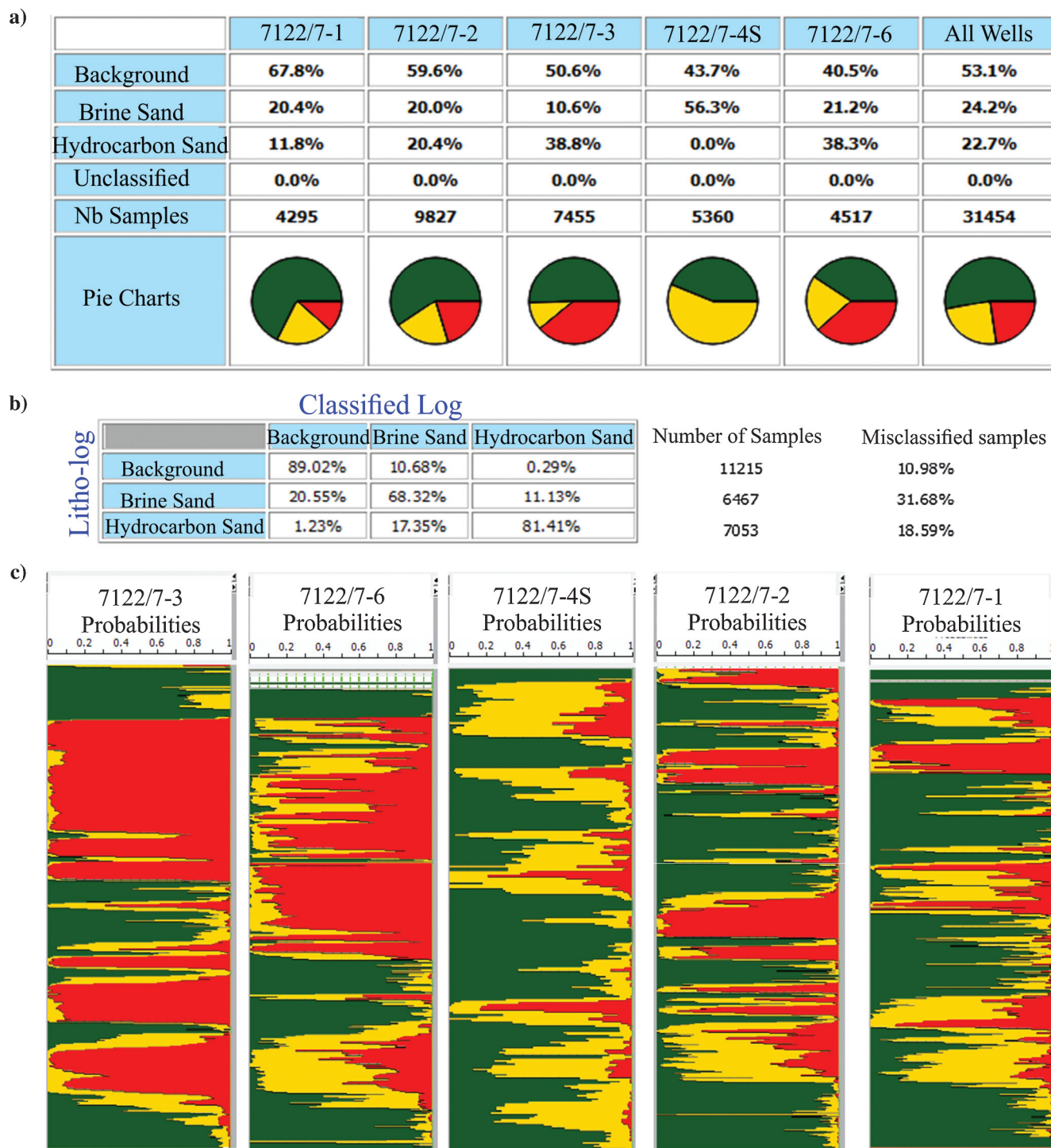
**Figure 14.** Lithology facies proportions and confusion matrix. The 7122/7-3 and the 7122/7-6 wells show a distinct proportion of clean sands. The facies proportion from all wells (a) provides the a priori facies proportions used in the Bayesian classification. The off-diagonal elements in the confusion matrix (b) show the degree of error.



sand-probability observations are supported by the scaled Poisson's ratio-AVA attribute (high Poisson's ratio in areas with low probability for sand). The relationship between the fan development and the relay-ramp structure may be indications of the onset of tectonic activity at the boundary fault (TFFC), which became more pronounced in the Mid-Jurassic times. It is expected that

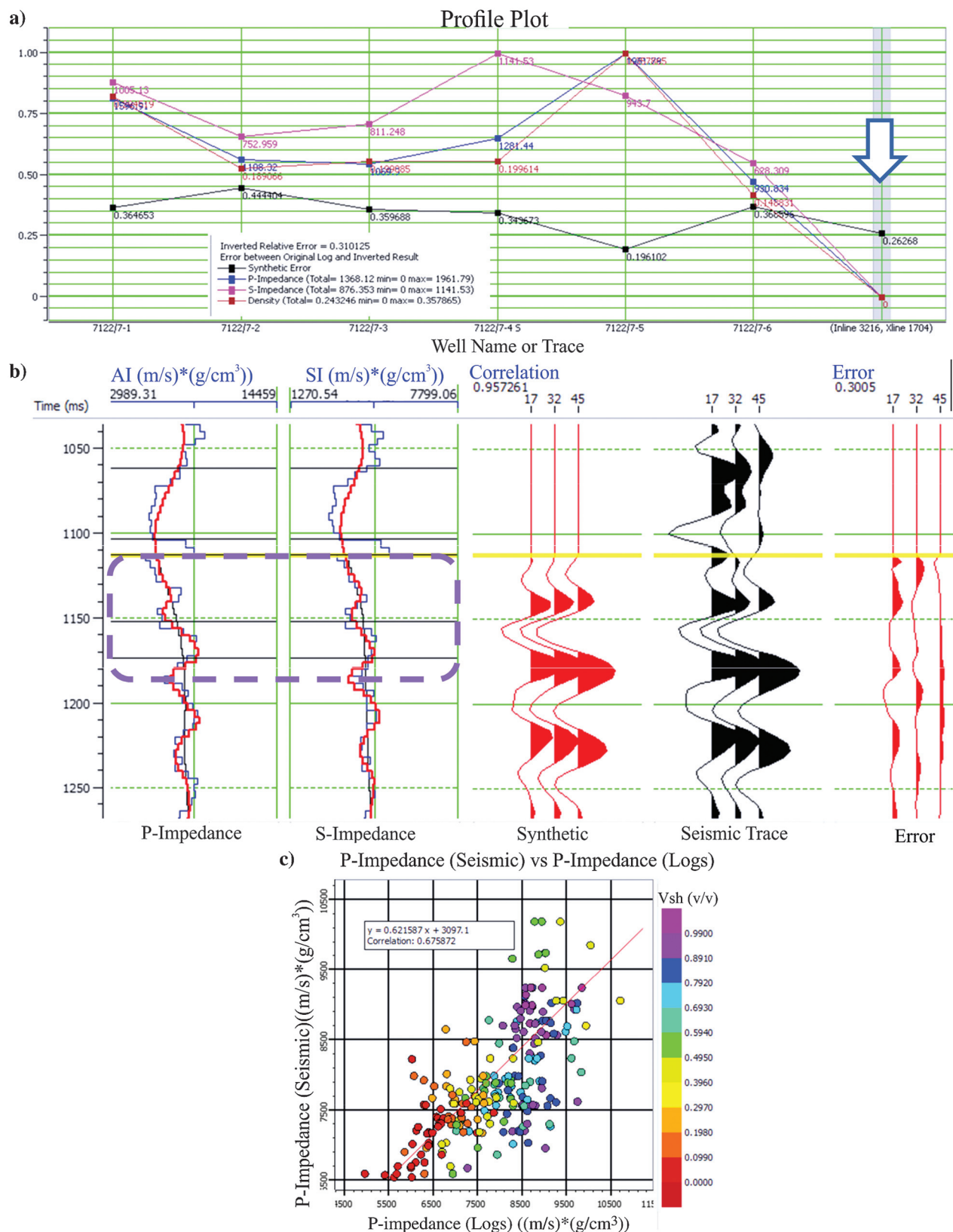
preexisting zones of weaknesses, such as the major TFFC, would respond first to rift initiation.

Figure 19 shows the results of the mixed lithology and fluid classification. The brine and hydrocarbon-sand probability horizon slices are taken 10 ms below the top of the reservoir and over a 10 ms window. These two slices show the average fluid probability response



**Figure 15.** Lithology and fluid-facies classification at the wells. Facies proportions in panel (a) provide the a priori probability of the different classes. (b) The confusion matrix shows the degree of classification error for each class from all the wells. (c) Meanwhile, the modeled facies probability tracks show the result of the classification in the well and modeled well probabilities.





**Figure 16.** Inversion error profiles across the wells and inversion quality control. The P-impedance, S-impedance, and density curves in panel (a) show the correlation to the actual logs. Meanwhile, the synthetic error curve (black) in panel (b) shows the error profile between the inverted seismic trace and the actual trace at the wells. A blind test synthetic error is also included (white arrow). The purple rectangle shows the target zone in the reference well. The red, blue, and black curves in the impedance log tracks represent the inverted log, actual log, and background model, respectively. The crossplot in panel (c) shows the correlation between the inverted P-impedance and the actual impedance.

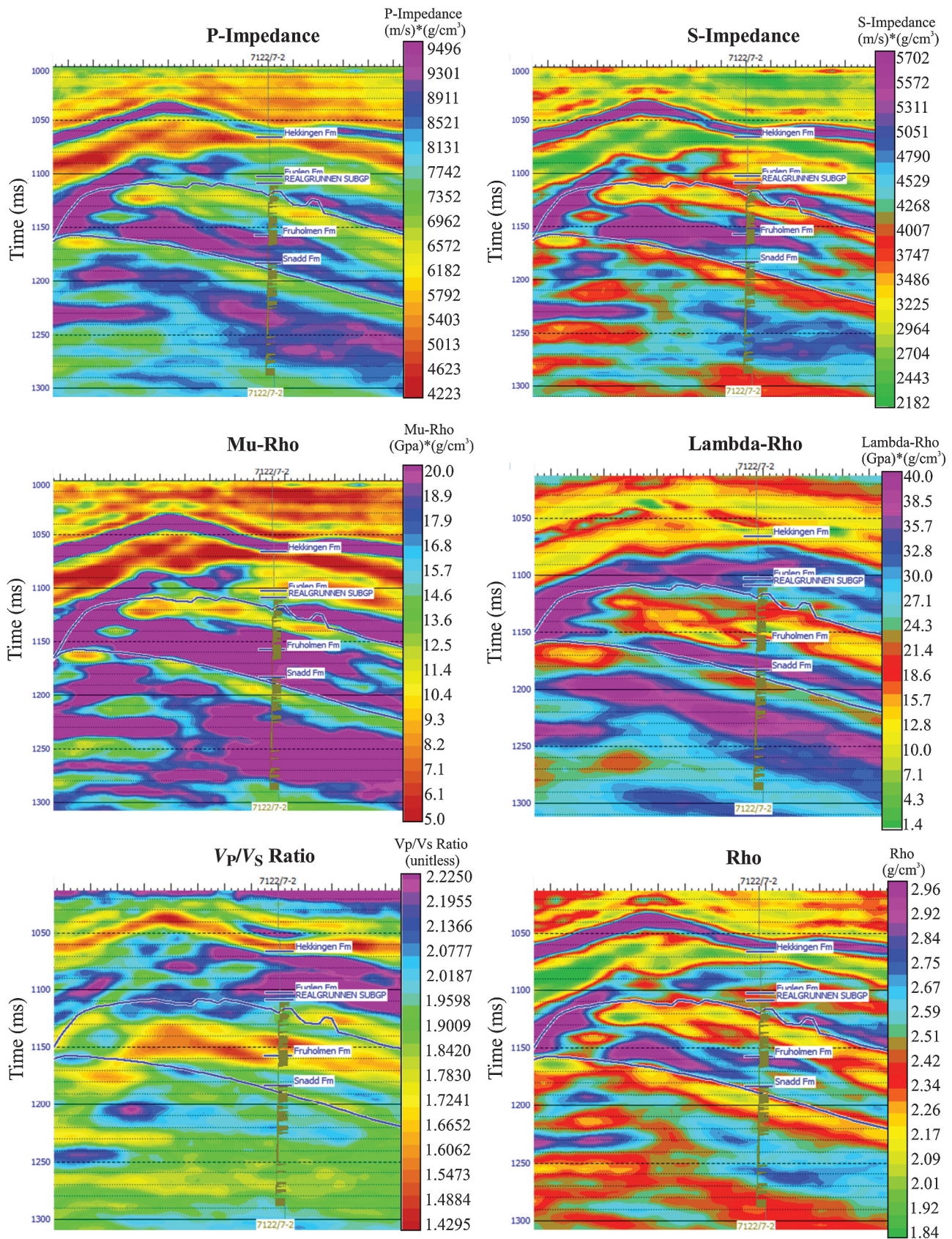


**Figure 17.** Simultaneous inversion results and computed LMR attributes. The low P-impedance in the source rock above the reservoir shows an opposite trend in the  $V_p/V_s$  ratio compared with the reservoir.



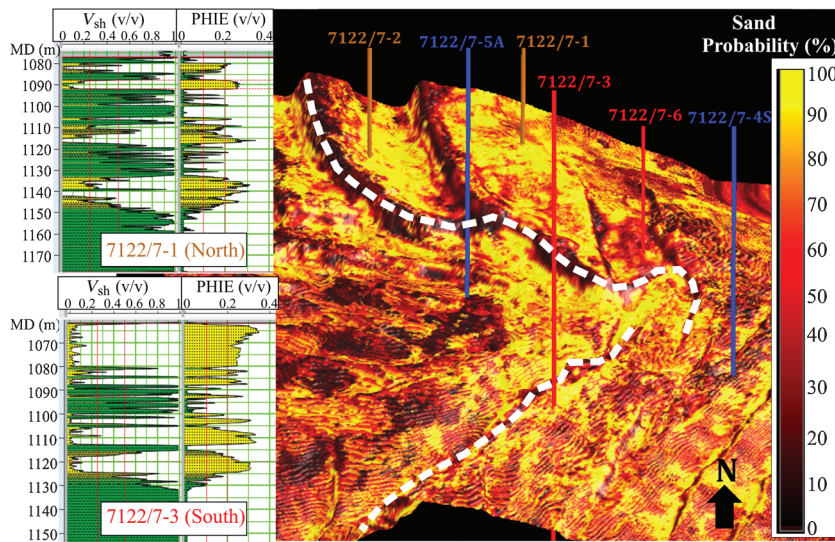


**Figure 18.** Sand-probability horizon slice taken 10 ms below top of the Realgrunnen Subgroup. The outline of a relay ramp fault is shown in white. Wells to the north tend to show a poor sand development at the top (e.g., 7122/7-1) but a wider lateral extent compared with the south (e.g., 7122/7-3).

in the top of the reservoir. It should be noted that a low brine-sand probability does not directly imply a high hydrocarbon probability for the same zone unless there is a corresponding low shale probability in the area of investigation. In the shale, brine-sand and hydrocarbon-sand probability inline sections of the 7122/7-2 well show an oil leg pinching out updip, which is most likely related to degrading reservoir quality (either higher  $V_{sh}$  or lower PHIE). The top of the Snadd Formation has brine-filled sands at the well location, but the hydrocarbon-sand probability inline section indicates an 80% chance of hydrocarbon sands down-dip in other compartments. This shows the potential of this method to highlight undrained pay sands.

One of the limitations in the simultaneous inversion used here is the assumed linear trend between  $\ln(AI)$  to  $\ln(SI)$  and

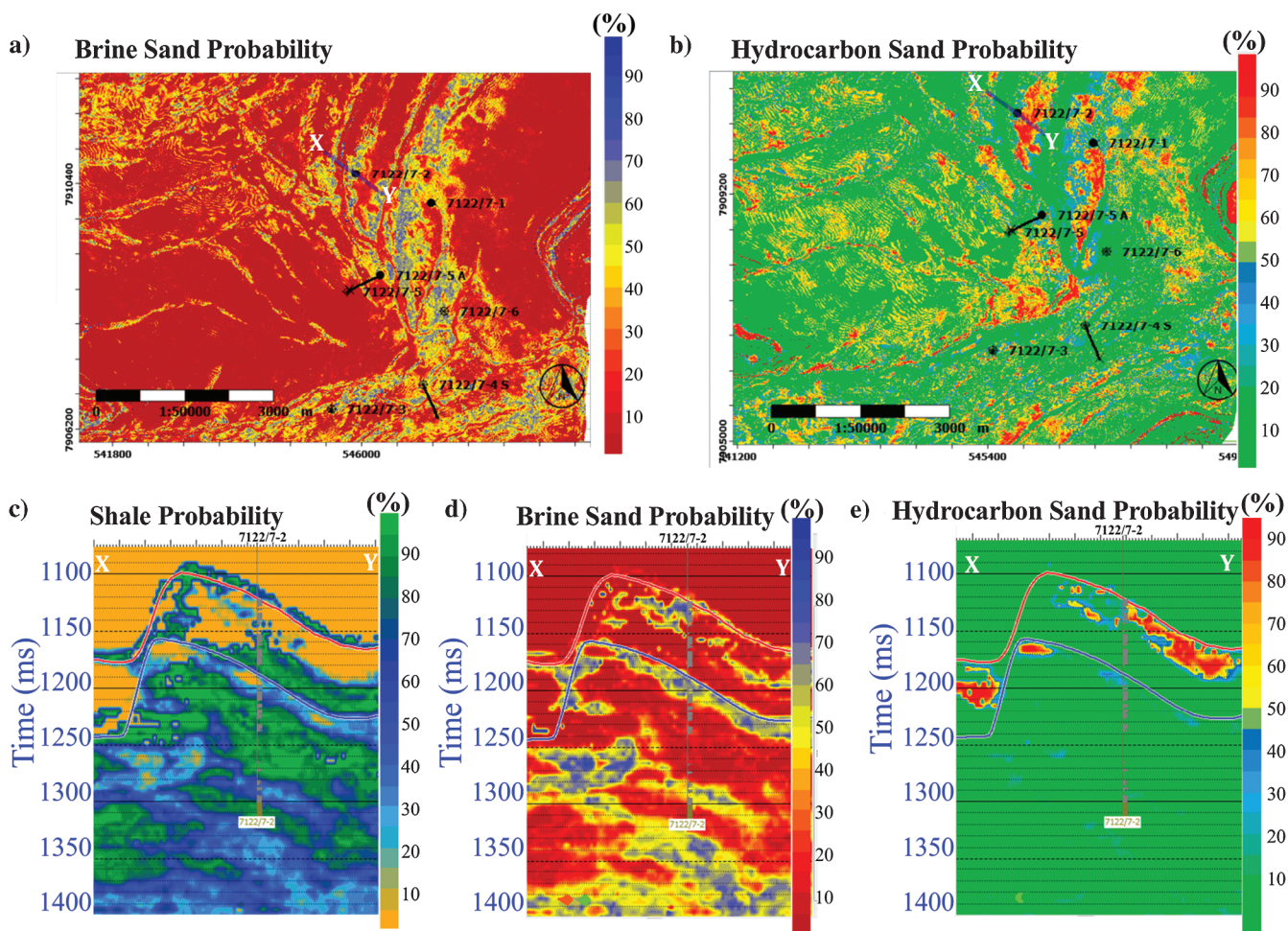


**Figure 19.** Facies probability horizon slices for (a) brine and (b) hydrocarbon sands. The corresponding inline sections (X-Y profile) across the 7122/7-2 well are also shown including a shale probability section.

$\ln(\rho)$ . In reality, more than one facies-dependent linear trend may be required. The background linear trend implemented in this work (Figure 9) shows a high correlation coefficient greater than 85% for the data points. However, a subordinate trend shown in white highlights the potential limitation of this method. If the correlation coefficient in the background linear trend is low, multiple trend lines should then be ideally included to capture the facies-dependent rock-physics relationship in the data. No sensitivity analysis has been conducted on the impact of background model. Despite this limitation, the simultaneous inversion results are still robust enough to capture the main sand depositional trends within the Realgrunnen reservoir. Cokriging the PSDM velocities with the well velocities during construction of the background low-frequency model played a role in stabilizing the model. A joint facies-based impedance inversion has been suggested (Kemper and Gunning, 2014), which takes into account facies depth trends when constructing a low-frequency background trend. Furthermore, no stochastic simulation has been performed to augment the well training data set for facies not encountered in the wells but which may be present in this depositional environment.

Based on the AVA analysis, an EEI approach for lithology prediction would work equally well for the Realgrunnen Subgroup. The optimum chi-angle projections for  $V_{sh}$  and PHIE show very good correlations. These two geologic variables have been used to define the rule-based facies used in this study. This demonstrates a positive feasibility of using EEI for lithology discrimination, but that was not the focus in this paper. In an exploration and field development context, it is important to focus on initial efforts to understand the spatial and temporal sand distribution before fluid anomaly scouting. This approach highlights the need to constrain lithology trends to identify the clean sands and then subsequently integrate a fluid discrimination criterion.

## Conclusion

AVA-attribute analyses revealed a class IV response for the top Realgrunnen reservoir in the study area. The suggested lithology and fluid prediction workflow for the reservoir zone in Realgrunnen Subgroup is dependent on the quality of the implemented simultaneous elastic inversion. A good elastic inversion result at the well locations improves the reliability of the lithology predictions. The simple rule-based ternary classifications used in this study can be applied to other seismic attribute vectors, provided that they show sufficient clustering in the petroelastic domain. The facies distribution patterns have been used to infer a possible influence of tectonic activity during deposition of the Realgrunnen Subgroup. However, more detailed structural interpretations need to be incorporated to ascertain this claim. The hydrocarbon-sand probability distribution maps can be used as input into reservoir-modeling workflows. These maps have the potential to guide the placement of injec-

tors and producers and, as a consequence, optimize the drainage for such compartmentalized heterogeneous reservoirs.

## Acknowledgments

This work is partially funded by the project "Reconstructing the Triassic Northern Barents shelf: Basin infill patterns controlled by gentle sags and faults" (Trias North) under grant no. 234152 from the Research Council of Norway and with financial support from Tullow Oil Norge, Lundin Norway, Statoil Petroleum, Edison Norge, and Dea Norge. The authors also thank Eni Norge and Statoil ASA of the PL229 license for permission to publish the data. This work has been carried out using the Hampson-Russell commercial software package at the University of Oslo. The authors would also like to acknowledge L. Nilssen (Statoil ASA), J. Leutscher (Eni Norge), F. Tsikalas (Eni Norge), and A. Onana (Lundin Petroleum) for fruitful discussions during the project and M. Heeremans (UiO) for data management and software support.

## References

- Aki, K., and P. G. Richards, 1980, Quantitative seismology: Theory and methods: W. H. Freeman.
- Aki, K., and P. G. Richards, 2002, Quantitative seismology, 2nd ed.: W.H. Freeman and Company. 5
- Buia, M., C. Cirone, J. Leutscher, S. Tarran, and B. Webb, 2010, Multi-azimuth 3D survey in the Barents Sea: First Break, **28**. 6
- Buland, A., and H. Omre, 2003, Bayesian linearized AVO inversion: Geophysics, **68**, 185–198, doi: [10.1190/1.1543206](https://doi.org/10.1190/1.1543206).
- Castagna, J., H. Swan, and D. Foster, 1998, Framework for AVO gradient and intercept interpretation: Geophysics, **63**, 948–956, doi: [10.1190/1.1444406](https://doi.org/10.1190/1.1444406).
- Dario, G., E. P. S. Mancini, and C. Tarchiani, 2013, Seismic driven probabilistic classification of reservoir facies for static reservoir modeling: A case history in the Barents Sea: Geophysical Prospecting, **61**, 613–629, doi: [10.1111/j.1365-2478.2012.01115.x](https://doi.org/10.1111/j.1365-2478.2012.01115.x).
- Dore, A. G., 1995, Barents Sea geology, petroleum resources and commercial potential: Arctic, **48**, 207–221, doi: [10.14430/arctic1243](https://doi.org/10.14430/arctic1243).
- Dvorkin, J., and A. Nur, 1996, Elasticity of high-porosity sandstones: Theory for two North Sea data sets: Geophysics, **61**, 1363–1370, doi: [10.1190/1.1444059](https://doi.org/10.1190/1.1444059).
- Faleide, J. I., S. T. Gudlaugsson, and G. Jacquart, 1984, Evolution of the western Barents Sea: Marine and Petroleum Geology, **1**, 123IN112IN5137–128IN4136IN8150, doi: [10.1016/0264-8172\(84\)90082-5](https://doi.org/10.1016/0264-8172(84)90082-5).
- Faleide, J. I., F. Tsikalas, A. J. Breivik, R. Mjelde, O. Ritzmann, Ø. Engen, J. Wilson, and O. Eldholm, 2008, Structure and evolution of the continental margin off Norway and the Barents Sea: Episodes, **31**, 82–91.
- Fatti, J. L., G. C. Smith, P. J. Vail, P. J. Strauss, and P. R. Levitt, 1994, Detection of gas in sandstone reservoirs



- using AVO analysis: A 3-D seismic case history using the Geostack technique: *Geophysics*, **59**, 1362–1376, doi: [10.1190/1.1443695](https://doi.org/10.1190/1.1443695).
- Gabrielsen, R. H., R. B. Færseth, L. N. Jensen, J. E. Kalheim, and F. Riis 1990, Structural elements of the Norwegian Continental Shelf. Part I: The Barents Sea Region: *NPD-Bulletin*, **6**, 33.
- Gassmann, F., 1951, Elastic waves through a packing of spheres: *Geophysics*, **16**, 673–685, doi: [10.1190/1.1437718](https://doi.org/10.1190/1.1437718).
- Glørstad-Clark, E., J. I. Faleide, B. A. Lundschieen, and J. P. Nystuen, 2010, Triassic seismic sequence stratigraphy and paleogeography of the western Barents Sea area: *Marine and Petroleum Geology*, **27**, 1448–1475, doi: [10.1016/j.marpetgeo.2010.02.008](https://doi.org/10.1016/j.marpetgeo.2010.02.008).
- Goodway, B., T. Chen, and J. Downton, 1997, Improved AVO fluid detection and lithology discrimination using Lamé petrophysical parameters, “ $\lambda\rho$ ,” “ $\mu\rho$ ,” and “ $\lambda/\mu$  fluid stack,” from P and S inversions: National Convention, Canadian Society of Exploration Geophysics, **22**, 183–186.
- Gradstein, F. M., J. G. Ogg, M. D. Schmitz, and G. M. Ogg, 2012, *The geological time scale 2012*: Elsevier.
- Hampson, D. P., B. H. Russell, and B. Bankhead, 2005, Simultaneous inversion of pre-stack seismic data: 75th Annual International Meeting, SEG, Expanded Abstracts, 1633–1636.
- 7** Johansen, S. E., B. K. Ostist, Ø. Birkeland, O. Cristensen, S. I. Cheredeev, E. A. Ignatenko, and M. Margulis, 1993, Hydrocarbon potential in the Barents Sea region: Play distribution and potential, in T. O. Vorren, et al., eds., *Arctic geology and petroleum potential*, NPF Special Publication: Elsevier, 273–320.
- Kemper, M., and J. Gunning, 2014, Joint impedance and facies inversion: Seismic inversion redefined: *First Break*, **32**, 89–95.
- Lancaster, S., and D. Whitcombe, 2000, Fast track “colored” inversion: 70th Annual International Meeting, SEG, Expanded Abstracts, 1572–1575.
- Mørk, A., A. F. Embry, and W. Weitschat, 1989, Triassic transgressive-regressive cycles in the Sverdrup Basin, Svalbard and the Barents Shelf, in C. D. Collinson, ed., *Correlation in hydrocarbon exploration*: Norwegian Society Conference, Graham and Trotman, 113–130.
- Ødegaard, E., and P. Avseth, 2004, Well log and seismic data analysis using rock physics templates: *First Break*, **22**, 37–43.
- Ohm, S. E., and D. A. Karlsen, 2008, Geochemically driven exploration models in uplifted areas: Examples from the Norwegian Barents Sea: *AAPG Bulletin*, **92**, 1191–1223, doi: [10.1306/06180808028](https://doi.org/10.1306/06180808028).
- Riis, F., B. A. Lundschieen, T. Hoy, A. Mork, and M. B. E. Mork, 2008, Evolution of the Triassic shelf in the northern Barents Sea region: *Polar Research*, **27**, 318–338, doi: [10.1111/j.1751-8369.2008.00086.x](https://doi.org/10.1111/j.1751-8369.2008.00086.x).
- Rutherford, S., and R. Williams, 1989, Amplitude-versus-offset variations in gas sands: *Geophysics*, **54**, 680–688, doi: [10.1190/1.1442696](https://doi.org/10.1190/1.1442696).
- Shuey, R. T., 1985, A simplification of the Zoeppritz equations: *Geophysics*, **50**, 609–614, doi: [10.1190/1.1441936](https://doi.org/10.1190/1.1441936).
- Whitcombe, D. N., P. A. Connolly, R. L. Reagan, and T. C. Redshaw, 2002, Extended elastic impedance for fluid and lithology prediction: *Geophysics*, **67**, 63–67, doi: [10.1190/1.1451337](https://doi.org/10.1190/1.1451337).
- Worsley, D., O. J. Aga, and A. Dalland, 1986, *The geological history of Svalbard: Evolution of an Arctic archipelago*: Den norske stats oljeselskap.
- Yenwongfai, H. D., N. H. Mondol, I. Lecomte, and J. I. Faleide, 2016, Prestack simultaneous inversion to predict lithology in the Realgrunnen Subgroup of the Goliat field, SW Barents Sea: 78th Annual International Conference and Exhibition, EAGE, Extended Abstracts, doi: [10.3997/2214-4609.201600964](https://doi.org/10.3997/2214-4609.201600964).
- Zoeppritz, K., 1919, *Erdbebenwellen VIII B: On the reflection and penetration of seismic waves through unstable layers*: Goettinger Nachrichten, **1**, 66–84.



#### Honore Dzekamelive Yenwongfai

received a B.S. (hons) in geology and chemistry from the University of Buea, Cameroon, an M.S. in petroleum geology and petroleum geophysics from the University of Oslo, Norway (Quota Scheme Grant), and a Ph.D. candidate (grants from Research Council of Norway and industry partners) in petroleum geophysics from the University of Oslo. He then joined Statoil ASA (2011) as a reservoir geologist in petroleum technology, and he is currently a senior geologist in reservoir characterization and modeling. His main research interests include seismic petrophysics and modeling for facies analysis.



#### Nazmul Haque Mondol

received a B. S. in geology (University of Dhaka, Bangladesh), an M.S. in geology (University of Dhaka, Bangladesh) and petroleum geosciences (NTNU, Norway), and a Ph.D. in experimental rock physics (University of Oslo, Norway). He is an associate professor at the University of Oslo and an advisor

(adjunct position) at Norwegian Geotechnical Institute, Oslo, Norway. He was postdoctoral fellow at the University of Oslo, Norway (grants from Research Council of Norway under the PETROMAKS program), before joining permanently as an associate professor at the University of Oslo. His research interests include rock physics, petrophysics, geomechanics, geophysics, and seismic to characterize source, reservoir, cap, and overburden rocks for exploration and exploitation of conventional and unconventional hydrocarbons, and geologic storage of CO<sub>2</sub>.



**Jan Inge Faleide** is a professor at Department of Geosciences, University of Oslo, where he also achieved his cand. real. (1981) and dr.scient. (1990) degrees. He has been project leader/PI for several interdisciplinary and international research projects focussing on the formation and evolution of sedimentary basins and continental

margins. Most of the studies have been located offshore Norway and carried out in close collaboration with the petroleum industry. In these, geophysical and geologic data have been integrated at various scales, and many studies involved numerical and analog modeling. He received StatoilHydro's Research Award in 2009. At present, he is affiliated with two research centers (the Centre for Earth Evolution and Dynamics and the Research Centre for Arctic Petroleum Exploration). He is a member of the Norwegian Academy of Science and Letters (DNVA), the Norwegian Academy of Technological Sciences (NTVA), and the Norwegian Scientific Academy for Polar Research.



**Isabelle Lecomte** received an M.S. (1987), a Civ. Eng. (1988), and a Ph. D. (1990; IFREMER grant), all in geophysics and all at the University of Strasbourg, France. She was a post-doctoral fellow at NORSAR, Norway (grants from EU, 1991; Research Council of Norway, 1992), before joining permanently as a principal research

geophysicist in R&D seismic modeling (1993–2016). She newly moved to the University of Bergen (2016–present) as an associate professor of reservoir geophysics. She is also an adjunct associate professor at the University of Oslo (2012–present) and a visiting associate professor at NORSAR (2016–present). She received the 2001 EAGE Loránd Eötvös award and the 2014 Norwegian Geophysical award. Her main research interests include seismic modeling and imaging, with applications to seismic reflection, refraction, tomography, resolution analyses, and simulation of PSDM.



# Queries

1. For authors Dzekamelive Yenwongfai, Mondol, and Lecomte, are both affiliations current? Or is one “formerly” and the other “presently”? Also, please check the affiliation details for all authors.
2. Please provide complete reference-list info for the citations of Smith and Gidlow (1987), Castagna and Swan (1997), Connolly (1999), and Verm and Hiltermann (1995), or may we delete these citations?
3. Please provide complete reference-list info for the citation of Gudlaugsson et al. (1998), or may we delete the citation?
4. Please provide complete reference-list info for the citations of Gardner et al. (1974) and Simmons and Backus (1996), or may we delete these citations?
5. Please provide an in-text citation for Aki and Richards (2002).
6. Please provide the page number for Buia et al. (2010).
7. Please provide the full list of editor names for Johansen et al. (1993).